CHEMISTRY OF MATERIALS

pubs.acs.org/cm

Article

Pore-Nanospace Engineering of Mixed-Ligand Metal−Organic Frameworks for High Adsorption of Hydrofluorocarbons and Hydrochlorofluorocarbons

Yang-Yang Xiong, Rajamani Krishna, Tony Pham, Katherine A. Forrest, Cheng-Xia Chen,* Zhang-Wen Wei, Ji-Jun Jiang, Hai-Ping Wang, Yanan Fan, Mei Pan,* and Cheng-Yong Su*

Cite This: *Chem. Mater.* 2022, 34, 5116−5124

Read Online

ABSTRACT: The isostructural mixed-ligand metal−organic frameworks (MOFs), LIFM-66, 66/67-mix, and 67, have been constructed via organic-linker modification and variation to introduce different portions of functional groups into the pore-nanospaces with tunable surface areas. Adsorption measurements of hydrofluorocarbon (HFC) and hydrochlorofluorocarbon (HCFC) with these MOFs reveal a record high uptake of R134a (1.09−1.14 g g^{-1}) and an ultrahigh uptake of R22 (0.85−0.96 g g^{-1}) under ordinary conditions of room temperature and atmospheric pressure. Noteworthily, the adsorption performance of greenhouse gases CO_2, R134a, and R22 can be finely regulated by introduced methyl groups, which has been elucidated by molecular modeling and transient breakthrough simulations/experiments, demonstrating an effective protocol of pore-nanospace engineering through rational design of mixed-ligand MOFs for HFC and HCFC capture, sequestration, and reclamation.

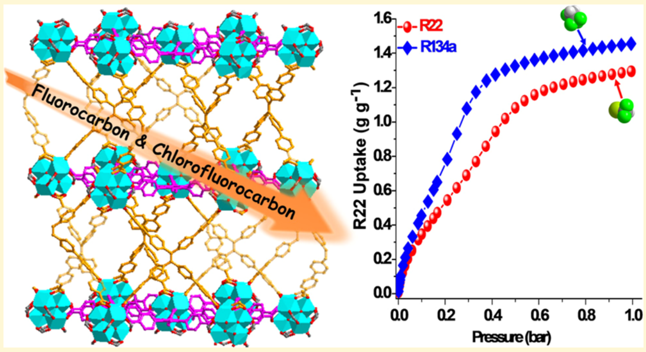

■ INTRODUCTION

The emission of greenhouse gases has given rise to irreversible damage to the global climate, threatening human daily life and health.[1] Although carbon dioxide (CO_2) is the arch-criminal at this stage because of its high emission levels, some other compounds present three or even four orders of magnitude higher global warming potentials (GWPs) per unit of mass.[2] Among them, the Freon gases like hydrofluorocarbons (HFCs) and hydrochlorofluorocarbons (HCFCs), that is, hydrocarbon derivatives in which one or more hydrogen atoms are substituted by fluorine and/or chlorine atoms, are a class of typical greenhouses species with an exceptionally high GWP.[3,4] Additionally, HFCs and HCFCs act as active ozone-depleting species, leading to a destructive effect on the ozone layer. Because of their significant environmental impact, the manufacture of HFCs and HCFCs has been gradually banned since the ratified Montreal Protocol. Nevertheless, the production of HFCs and HCFCs has never been completely phased out because of their practical and industrial relevance to the fields including but not limited to refrigerants, propellants, foams, fluoropolymers, solvents, cleaning agents, and so on.[5−8] In fact, although the consumption and production of HFCs and HCFCs have been strictly regulated, the operation and maintenance of existing equipment that use these refrigerants is going to last for a long time, and the emission of HFCs or HCFCs from the fluorine chemical industry is inevitable. Therefore, their capture, sequestration, and reclamation are of great significance for global environmental concerns.[9−12] Moreover, the determination of HCFCs and HFCs in air and seawater is important in environmental and geochemical analyses; however, their low concentration level in the atmosphere causes a difficulty in detection. An implementable method is to gather HCFCs and HFCs from the air or indoor environments through a column enrichment approach for accuracy detection,[13−15] which requires adequate adsorbent materials to effectively capture and concentrate HCFCs and HFCs under ordinary laboratory conditions.

Porous solids have been proved to be effective adsorbents for capturing and removing hazardous gases because of their porosity and high surface area.[10,16,17] Nevertheless, traditional porous materials like activated carbons, silica gels, and zeolites often suffer from a lack of selectivity, tunability, functionalization ability, and low porosity. Metal−organic frameworks (MOFs), as a new class of porous crystalline materials, have

Received: February 24, 2022
Revised: May 11, 2022
Published: May 25, 2022

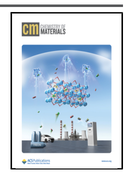

https://doi.org/10.1021/acs.chemmater.2c00601
Chem. Mater. 2022, 34, 5116−5124

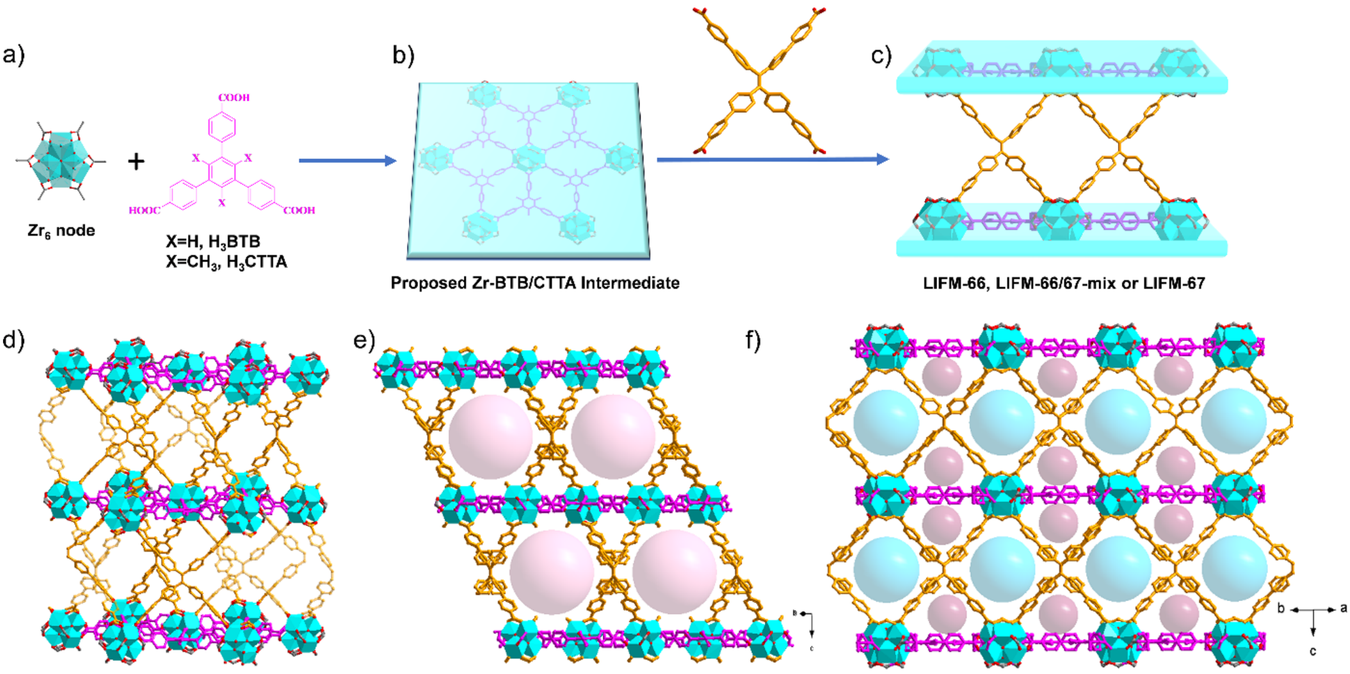

Figure 1. Synthetic procedure and crystal structure of LIFM-66, 66/67-mix, and 67. (a) Zr_6-node and H_3BTB/H_3CTTA linkers; (b) Zr-BTB/CTTA intermediate; (c) structure of LIFM-66, 66/67-mix, and 67 showing layers and pillars; (d) packing mode; (e) straight hexagonal channels along the *a*-axis; and (f) square and triangle channels along the *b*-axis. Color scheme: pink, BTB/CTTA linker; yellow, ETTC pillar; cyan, Zr_6-node; magenta, hexagonal channel; light cyan, square channel; purple, triangle channel.

presented great potential in gas adsorption owing to their highly tunable nature referring to structural topology, composition, porosity, and functionalization.[18−21] So far, a lot of effort has been devoted to improving the enrichment and separation of gases for recycling usage through diversified crystal engineering strategies, such as incorporating unsaturated metal sites,[22−24] tuning pore size/shape via pore engineering,[25−27] and functioning organic-linkers via appropriate groups.[28−30] Among them, the incorporation of open metal centers and the increase of the pore volume/surface area are the most used strategies for Freon gas adsorption.[9−11,31−36] However, the strong gas−framework interactions enforced by the open metals usually impart strong affinities toward Freon gases, but at the same time, adversely reduce the adsorption selectivity, whereas the high pore volume can endow the MOFs with better adsorption capacity under high pressure, but might not under ordinary conditions with low pressure. Functionalization of the organic-linkers presents another alternative method to improve Freon gas adsorption; for example, the fluorinated MOFs have been proven an appealing platform for the adsorption of HCFCs and HFCs.[9,37−40] Recently, organic variation and functionalization of MOFs have been extensively applied since the pioneering studies from Yaghi,[41−43] Zhou,[44,45] and other groups,[46−52] demonstrating that the pore-nanospace engineering via introducing functional variates to adjust pore environments is an effective approach to enhance gas adsorption properties. However, this strategy with variation of functionalized organic-linkers is still rarely applied in modulating the adsorption behavior of Freon gases, which may provide an effective way to balance the gas affinity with a high pore volume for low-pressure adsorption and separation performance.

Herein, we report a mixed-ligand MOF series, LIFM-66, 66/67-mix, and 67 (LIFM stands for Lehn Institute of Functional Materials) as shown in Figure 1, which manifest the best capture ability of R134a (CH_2FCF_3) surpassing all other known MOFs and that of R22 ($CHClF_2$) comparable with the record holder MOF at 298 K and 1 bar. Moreover, these mixed-ligand MOFs show high adsorption selectivity of R22/R134a over N_2 based on ideal adsorbed solution theory (IAST) calculations and transient breakthrough simulation and fast adsorption kinetics. Noteworthily, R22 and R134a adsorption properties can be finely tuned by modification of pore environments through variation of organic-linkers, proving effectiveness of pore-nanospace functionalization for HFC and HCFC capture and sequestration. Molecular modeling demonstrates a distinct mechanism for HFC and HCFC uptake, in which the O···H, F···H, and Cl···H interactions and other weak van der Waals forces on the pore surface play a synergetic role in HFC and HCFC adsorption.

■ EXPERIMENTAL SECTION

Synthesis of LIFM-66. LIFM-66 was prepared from a modified procedure reported previously.[52] H_3BTB (50 mg), $ZrCl_4$ (150 mg), and DMF (10 mL) were charged in a vial. The mixture was sonicated for 10 min and then heated in an 85 °C oven for 2 h. After cooling down to room temperature, H_4ETTC (50 mg) and benzoic acid (3.5 g) dissolved in DMF (5 mL) were added to the vial. The mixture was heated in a 120 °C oven for 5 days, and colorless hexagonal crystals were harvested (48.6 mg, 35.2%). FTIR (cm^{-1}): 3368 (w), 3031 (w), 2989 (w), 2075 (w), 2014 (w), 1945 (w), 1705 (m), 1650 (m), 1589 (s), 1532 (s), 1403 (s), 1278 (m), 1179 (m), 1103 (m), 1005 (m), 969 (m), 867 (m), 969 (m), 834 (m), 782 (m), 752 (m), 714 (m), 635 (s), 564 (w).

Synthesis of LIFM-66/67-Mix. H_3BTB (20 mg), H_3CTTA (30 mg), $ZrCl_4$ (150 mg), and DMF (10 mL) were charged in a vial. The mixture was sonicated for 10 min and then heated in an 85 °C oven for 2 h. After cooling down to room temperature, H_4ETTC (50 mg) and benzoic acid (3.5 g) dissolved in DMF (5 mL) were added to the vial. The mixture was heated in a 120 °C oven for 5 days, and

https://doi.org/10.1021/acs.chemmater.2c00601
Chem. Mater. 2022, 34, 5116−5124

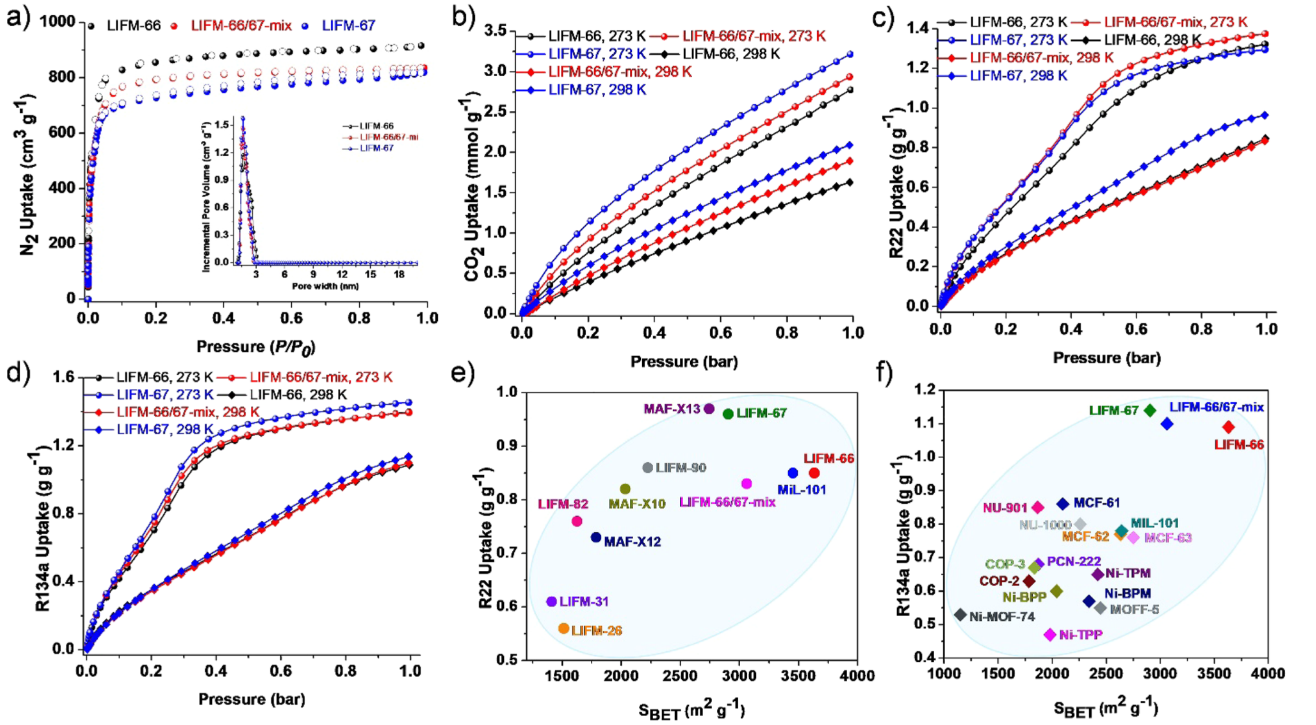

Figure 2. (a) N_2 adsorption at 77 K with the inset showing distribution of pore sizes. (b−d) CO_2, R22, and R134a adsorption isotherms at 273 and 298 K. (e) Comparison of the BET surface area and R22 uptake at 298 K and 1 bar between the top-performing MOFs and our cases. (f) Comparison of the BET surface area and R134a uptake at 298 K and 1 bar between the top-performing MOFs and our cases.

colorless hexagonal crystals with different linker ratios were harvested (57.3 mg, 44.1%). FTIR (cm^{-1}): 3362 (w), 3038 (w), 2989 (w), 2009 (w), 1938 (w), 1701 (m), 1650 (m), 1590 (s), 1533 (s), 1402 (s), 1179 (m), 1146 (m), 1102 (m), 1005 (m), 855 (m), 836 (m), 781 (s), 752 (m), 712 (m), 631 (s).

Synthesis of LIFM-67. H_3CTTA (50 mg), $ZrCl_4$ (150 mg), and DMF (10 mL) were charged in a vial. The mixture was sonicated for 10 min and then heated in an 85 °C oven for 2 h. After cooling down to room temperature, H_4ETTC (50 mg) and benzoic acid (3.5 g) dissolved in DMF (5 mL) were added to the vial. The mixture was heated in a 120 °C oven for 3 days, and colorless hexagonal crystals were harvested (53.8 mg, 39.0%). FTIR (cm^{-1}): 3368 (w), 3220 (w), 3070 (w), 2123 (w), 2014 (w), 1945 (w), 1812 (w), 1692 (m), 1589 (s), 1532 (s), 1403 (s), 1179 (m), 1146 (m), 1107 (m), 1005 (m), 855 (s), 777 (s), 702 (m), 635 (s).

Computational Methods. The binding sites for $CHClF_2$ and CH_2FCF_3 in LIFM-66 and LIFM-67 were determined through classical molecular simulations (see details in Supporting Information S16). The X-ray single-crystal crystallographic data were used to perform the parametrizations and simulations.

■ RESULTS AND DISCUSSION

Synthesis and Crystal Structure. LIFM-66, 66/67-mix, and 67 are constructed from a Zr_6-node and three variant organic linkers, 1,3,5-benzenetrisbenzoate (H_3BTB), 5′-(4-carboxyphenyl)-2′,4′,6′-trimethyl-[1,1′,3′,1″-terphenyl]-4,4″-dicarboxylic acid (H_3CTTA), and 4′,4‴,4⁗′,4″‴′-(ethene-1,1,2,2-tetrayl)tetrakis ([1,1′-biphenyl] -4-carboxylate) (H_4ETTC), as isostructures (Figure 1 and Scheme S1). LIFM-66 is obtained through a slightly modified process reported previously.[52] The reaction of triangular linker H_3BTB and $ZrCl_4$ probably affords a two-dimensional (2D) Zr-BTB intermediate first, and then tetrapodal linker H_4ETTC as the pillar is added into the reaction system to produce three-dimensional (3D) LIFM-66 (Figure 1), giving hexagonal crystals as an isostructure of PCN-134.[50] The crystal structure contains a (3,6)-connected **kgd** 2D layer formed by BTB linkers and Zr_6-nodes, while ETTC linkers serve as crosslinking pillars to extend the layers into a (3,4,10)-connected 3D net of $\{4^{16}\ 6^{20}\ 8^9\}\{4^3\}_2\{4^4\ 6^2\}$ point symbol. As the MOF is constructed by strong Zr−O bonds via high 10-connectivities, it possesses extraordinary stability to sustain growth of imperfect and defective crystalline solids to a certain extent, which is evident from the fact that, although a theoretical 1:2 ratio of ETTC: BTB is used in the synthesis, the ^1H NMR determination of the digested sample reveals an actual 1:1.54 ratio (Figure S1 and Table S2), suggesting the existence of defects due to the proportional lack of BTB linkers.

Considering the hydrophobic nature of HFCs and HCFCs, methyl-functionalized CTTA linkers are chosen to partially or completely replace the BTB linkers in the 2D layers of LIFM-66. As a consequence, two new porous isostructural MOFs, namely, LIFM-66/67-mix and LIFM-67, are obtained. In LIFM-66/67-mix, the ratio of ETTC: (BTB + CTTA) is determined by ^1H NMR to be 1:1.63 (Figure S2 and Table S2). The total replacement of BTB linkers by CTTA in LIFM-67 is confirmed by the single-crystal X-ray diffraction analysis (Table S1), and the ^1H NMR experiment reveals an actual ETTC: CTTA ratio of 1:1.73 (Figure S3 and Table S2), slightly lower than the theoretical ratio of 1:2. The non-stoichiometric organic components in these mixed-ligand MOFs imply that some ETTC linkers are inserted between 2D layers with only one or two carboxylate groups attached to the Zr_6-nodes. Noticeably, the ratios of ETTC: (BTB + CTTA) get closer to the theoretical 1:2 ratio from LIFM-66 to LIFM-66/67-mix and LIFM-67 as the methyl groups are increased, suggesting that the crystal defect can be effectively reduced by introducing more methyl groups (Figures S1−S3 and Table S2). In all three MOFs, there exist various channels with different shapes and sizes along *a*- and *b*-axes (Figure

https://doi.org/10.1021/acs.chemmater.2c00601
Chem. Mater. 2022, 34, 5116−5124

1e,f). The aperture of the hexagonal channel along the *a*-axis is about 15.9 × 14.8 Å^2 (Figure 1e), while those of square and triangle channels along the *b*-axis are about 10.9 × 10.5 and 8.4 × 11.7 Å^2, respectively (Figure 1f).

Phase Purity and Porosity. Scanning electron microscopy (SEM) discloses that these mixed-ligand MOFs have similar hexagonal morphology (Figure S4). Powder X-ray diffraction (PXRD) verifies their phase purity and identity (Figures S5−S7). The thermogravimetric analyses are conducted to evaluate their thermal stability, indicating that they are stable up to 450 °C (Figure S8). To evaluate the porosity, N_2 adsorption of desolvated samples is measured for LIFM-66, 66/67-mix, and 67 at 77 K, all displaying type-I adsorption isotherms with saturated uptakes of 916, 836, and 819 cm^3 g^{-1}, indicative of the Brunauer−Emmett−Teller (BET) surface areas of 3631, 3176, and 2904 m^2 g^{-1}, respectively (Figures 2a, S9−S11 and Table S3). In addition, their total pore volumes are 1.42, 1.30, and 1.27 cm^3 g^{-1} (Table S3), respectively, higher than those of many known microporous MOFs with mixed organic linkers.[39,40,43,44,47,48,50,51] Their pore sizes calculated by the DFT method are 16.2, 15.6, and 15.5 Å, matching well with the crystal structure analysis results (Figure 2a insert). Noteworthily, the BET surface areas and pore volumes gradually decrease from LIFM-66 to 66/67-mix and LIFM-67 owing to the increase of the introduced methyl groups. Similar to LIFM-66 described in our previous work,[52] the chemical stability of LIFM-66/67-mix and LIFM-67 is confirmed by immersing the fresh samples in aqueous solutions at different pH values for 48 h, and the structural integrity and crystallinity are verified by the PXRD patterns to confirm their high stability in harsh chemical environments (Figures S12 and S13).

Greenhouse Gas Adsorption. Based on the high stability and porosity of these mixed-ligand MOFs, CO_2 adsorption measurements are first carried out to evaluate their performance in greenhouse gas capture and sequestration related to global warming. The CO_2 adsorption was conducted at 273, 285, and 298 K (Figures S14−S16), revealing a noticeable increase of CO_2 uptake with the increase of methyl-functionalized groups from LIFM-66 to LIFM-66/67-mix and LIFM-67. The CO_2 uptake of LIFM-66 reaches 36.5 cm^3 g^{-1} (1.6 mmol g^{-1}) at 298 K, which is further enhanced to 42.4 and 46.9 cm^3 g^{-1} (1.9 and 2.1 mmol g^{-1}) with LIFM-66/67-mix and LIFM-67, respectively (Figure 2b). These observations imply that the introduction of more methyl groups onto the pore surface can effectively improve gas−framework interactions, thus enhancing CO_2 sequestration. To verify this assumption, the virial fitting method is employed to fit the CO_2 adsorption data at different temperatures and the Clausius−Clapeyron equation is used to calculate the isosteric heat of adsorption (Q_{st}) (Figures S30−S32). For LIFM-66, Q_{st} is estimated to be 20.4 kJ mol^{-1}, whereas the values for LIFM-66/67-mix and LIFM-67 are calculated to be 36.3 and 31.6 kJ mol^{-1} (Figure S39), respectively, suggesting the enhancement of gas−framework interactions in mixed-ligand MOFs by virtue of methyl functionalization.

Noteworthily, this mixed-ligand MOF series display exceptionally high adsorption of Freon gases as represented by R22 and R134a (Figures 2c,d and S17−S22). For R22, LIFM-66/67-mix exhibits somewhat higher uptake at 273 K while LIFM-67 shows better uptake at 298 K, suggesting enrichment of R22 in the methyl group-modified pore-nanospaces. The higher adsorption of R22 by LIFM-67 at 298 K may be owing to the finding that the adsorbate−framework interactions tend to be enhanced while the adsorbate−adsorbate interactions tend to be weakened at a higher temperature.[11] Overall, extraordinary R22 adsorption capacities of these mixed-ligand MOFs are achieved, reaching 219.4 cm^3 g^{-1} (9.8 mmol g^{-1} or 0.85 g g^{-1}), 216.1 cm^3 g^{-1} (9.6 mmol g^{-1} or 0.83 g g-^{1}), and 249.8 cm^3 g^{-1} (11.2 mmol g^{-1} or 0.96 g g^{-1}) at 298 K and 1 bar (Figure 2e and Table S4), which outperform those of most reported MOFs[11,39,40,51] with LIFM-67 catching up with the benchmark MAF-13 (0.97 g g^{-1}).[31] As for R134a, LIFM-67 exhibits slightly higher uptake than the other two analogues (Figures 2d and S20−S22). Excitingly, until now the best R134a capture capability at 298 K and 1 bar has been observed by these mixed-ligand MOFs, giving uptake values of 238.5 cm^3 g^{-1} (10.6 mmol g^{-1} or 1.09 g g^{-1}), 241.5 cm^3 g^{-1} (10.8 mmol g^{-1} or 1.10 g g^{-1}), and 249.6 cm^3 g^{-1} (11.1 mmol g^{-1} or 1.14 g g^{-1}), remarkably surpassing the record holder MCF-61[32] and other reported MOFs under the same conditions (Figure 2f and Table S5).[11,32−37] The high-pressure R134a adsorption by LIFM-66 and LIF-67 is measured at 298, 313, and 333 K (Figures S26 and S27), revealing that LIFM-67 presents better R134a uptake behavior than LIFM-66. LIFM-66 can take up 1.35 and 1.11 g g^{-1} of R134a at 298 and 333 K under 6 bar, respectively, whereas the corresponding uptakes by LIFM-67 reach 1.48 and 1.23 g g^{-1}. It should be noted that, at this high pressure, the R134a adsorption of these mixed-ligand MOFs is lower than those of the benchmark MOFs like Ni-TPM (1.4 g g^{-1}),[33] NU-1000(Zr) (170 wt %),[36] and MIL-101(Cr) (140 wt %)[36] with relatively smaller pore surface areas but larger pore volumes (Table S5). This means that the R134a adsorption at high pressure with a saturation capacity is more related to the pore volume character rather than the pore surface area of MOFs, probably because of the propensity of fluorocarbons to be able to self-associate into the fluorous phase in the pores around the saturation pressure.[53] However, the capture capability at room temperature and atmospheric pressure is expected to more depend on the high pore surface area of MOFs, which can provide more gas−framework interacting places but not necessarily high condensation volume. Additionally, the repeating R134a adsorption experiments with LIFM-66 and LIFM-67 are carefully performed at 298 K (Figures S28 and S29), which confirm excellent durability of these MOFs for R134a capture without any loss of adsorption efficiency in three successive recycling tests. These results manifest that these mixed-ligand MOF series are excellent HFC and HCFC adsorption and sequestration candidates under ordinary conditions, owing to organic variation and functionalization beneficial for pore environment improvement. We can see from Figure 2e,f that the R22 and R134a uptake capacities at 298 K and 1 bar are generally in line with the BET surface areas of MOFs, but deviation to some extent is obvious as the molecular nature of the pore surfaces is varied, manifesting a synergistic effect from the pore-nanospace engineering contributed by both the surface area and functionalization.

We further employ the Clausius−Clapeyron equation to calculate R22 and R134a isosteric heats of these mixed-ligand MOFs on the basis of their adsorption isotherms measured at 273, 298, and 313 K (Figures S17−S22 and S33−S38). The R22 isosteric heat of LIFM-66 is 27.9 kJ mol^{-1} at zero coverage, while those of LIFM-66/67-mix and LIFM-67 are 36.1 and 36.2 kJ mol^{-1} (Figure S40), respectively, which are comparable with those of MIL-101 (34.6 kJ mol^{-1})[11] and some reported MOFs for R22 adsorption (Table

https://doi.org/10.1021/acs.chemmater.2c00601
Chem. Mater. 2022, 34, 5116−5124

S4)[31,39,40,48,51] and much higher than that of activated carbon (22.0−28.0 kJ mol^{-1}).[54] The R134a isosteric heats of these MOFs are 35.7, 37.9, and 38.9 kJ mol^{-1} at zero coverage, which are slightly higher than that of NU-1000 (32 kJ mol^{-1})[36] but lower than those of some reported MOFs for R134a adsorption (Figure S41 and Table S5).[34] These observations indicate that the methyl functionalization of the pore surface can improve the gas−framework interactions, thereon able to collaborate with the high pore surface area arisen from the mixed-ligand modification to efficiently enhance the Freon gas capture under ordinary conditions. The higher isosteric heats of R134a than R22 can be explained by their different boiling points, that is, the higher boiling point a gas has, the stronger gas···gas interactions there are, which are also observed with other gases like CO_2, N_2, and CH_4.[11]

To gain further insight into R22 and R134a uptake behaviors, molecular modeling has been implemented for LIFM-66 and LIFM-67, which reveals distinct adsorption mechanisms (Figure 3). In both MOFs, the R22 guest is

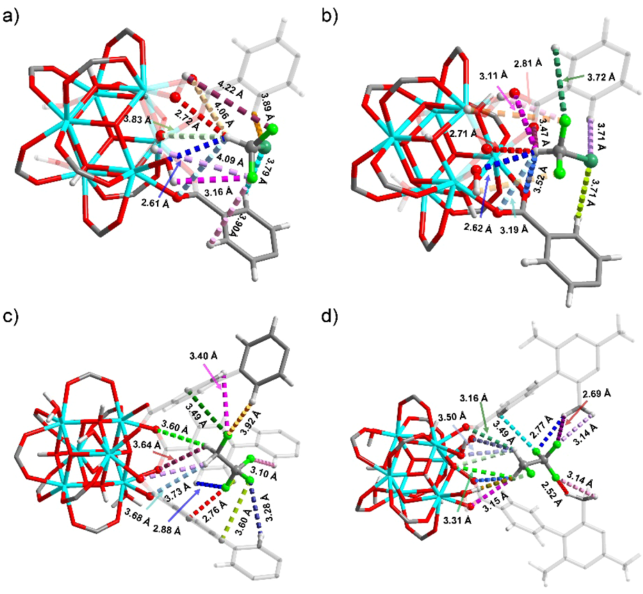

Figure 3. (a, b) Preferential R22 binding sites in LIFM-66 (left) and LIFM-67 (right) observed in the modeling study. (c, d) Preferential R134a binding sites in LIFM-66 (left) and LIFM-67 (right) observed in the modeling study.

located in a similar pocket surrounded by one Zr_6-cluster and two BTB/CTTA ligands (Figure 3a,b). Strong O···H−C_{FC} and O−H···F_{FC} interactions (2.61, 2.72, and 3.16 Å) and weak van der Waals forces (C−H···F_{FC} and C−H···Cl_{FC} ranging from 3.79 to 4.22 Å) are observed between R22 and the LIFM-66 framework, while the R22 guest interacts with the LIFM-67 framework through strong O···H−C_{FC} interactions (2.62, 2.71, 2.81, 3.11, and 3.19 Å) and weak C−H···F_{FC} and C−H···Cl_{FC} van der Waals forces ranging from 3.47 to 3.72 Å. The calculated R22 binding energy in LIFM-66 is 35.5 kJ mol^{-1}, while that in LIFM-67 is 42.8 kJ mol^{-1} (Table S8), indicative of stronger R22-framework interactions in LIFM-67 than that in LIFM-66. In contrast, the R134a guest is adsorbed by LIFM-66 and LIFM-67 within different environments (Figure 3c,d). In LIFM-66, R134a is located in a pocket composed of one Zr_6-cluster, two BTB ligands, and one ETTC linker, where strong C−H···F_{FCF} interactions (2.76, 2.88, and 3.10 Å) and weak van der Waals forces (O···H−C_{FCF} and C−H···F_{FCF} ranging from 3.28 to 3.92 Å) occur between R134a and the LIFM-66 framework. In LIFM-67, R134a is located in a pocket surrounded by one Zr_6-cluster and two CTTA ligands, where strong C−H···F_{FCF} interactions (2.52, 2.69, 2.77, 3.14, and 3.16 Å) and weak O···H−C_{FCF} and C−H···F_{FCF} van der Waals forces in the range of 3.31−3.49 Å happen between R134a and the LIFM-67 framework. The calculated R134a binding energy in LIFM-66 is 45.1 kJ mol^{-1}, whereas that in LIFM-67 is 46.7 kJ mol^{-1} (Table S8). These molecular modeling results suggest that stronger gas−framework interactions take place through introduction of methyl groups into the pore-nanospaces, generally in agreement with the experimental evidence derived from the gas adsorption calculations.

Greenhouse Gas Isolation and Concentration. The capture of greenhouse gases from the air or indoor environments using MOFs, especially for HCFCs and HFCs with low concentration, depends on the adsorption selectivity of these gases from the main air component like N_2 which is also frequently used as the carrier and purge gas in detection analysis. Therefore, we simply evaluate the isolation and concentration capability of these mixed-ligand MOFs for CO_2, R22, and R134a separation from N_2. The N_2 adsorption measurements disclose negligible uptakes of 5.2, 8.0, and 6.2 $cm^3\ g^{-1}$ (0.23, 0.35, and 0.27 mmol g^{-1}) at 298 K and 1 bar by LIFM-66, 66/67-mix, and 67 (Figures 4 and S23−S25), respectively. The IAST[55,56] model is used to estimate the CO_2/N_2 (15:85) separation property, offering selectivity values of 9, 7, and 12 at 298 K and 1 bar, respectively (Figure S52), suggesting that these mixed-ligand MOFs are good candidates for N_2 isolation and CO_2 sequestration under ambient conditions. Similarly, IAST calculations for R22/N_2 and R134a/N_2 separation with mixing ratios of 1:99 and 10:90 are performed (Figures 4c,d, S53, and S54). At 298 K and 1 bar, the performance of LIFM-66, 66/67-mix, and 67 for R22/N_2 and R134a/N_2 isolation in a 1:99 mixture is excellent with the selectivities calculated to be 186, 89, and 154 for R22/N_2 (Figure 4c) and 232, 100, and 154 for R134a/N_2 (Figure 4d) respectively. Similarly, all three MOFs exhibit high R22/N_2 and R134a/N_2 selectivities in 10:90 mixture (Figures S53 and S54). These separation selectivities for R22/N_2 and R134a/N_2 are outstanding among known MOFs,[39,48,51] suggesting promising usage of this mixed-ligand MOF series in HFC and HCFC isolation. It is noteworthy that these MOFs display superior isolation performance of R22/N_2 and R134a/N_2 in the low concentration of HFCs and HCFCs, showing much improved selectivities for the 1:99 mixture in comparison with the 10:90 mixture, indicating that these mixed-ligand MOFs have strong ability to capture and concentrate HFCs and HCFCs from the main air to facilitate detection and sequestration processes.

Inspired by the excellent R22 and R134a adsorption and the high R22/N_2 and R134a/N_2 selectivities, we carry out the simulated transient breakthrough experiments with 1:99 (v:v) and 10:90 (v:v) mixtures of R22/N_2 and R134a/N_2 according to the documented method.[57−59] As seen from Figures 4e,f, S55, and S56, N_2 elutes first in all cases, while R22 or R134a breaks after a remarkably delayed time, demonstrating adequate R22/N_2 or R134a/N_2 isolation and concentration ability. On the basis of the simulated breakthrough curves, the R22 capture capacity of LIFM-66 for 1:99 and 10:90 mixtures of R22/N_2 is calculated to be 0.19 and 1.50 mol kg^{-1}, respectively, whereas those values of LIFM-67 are 0.23 and

https://doi.org/10.1021/acs.chemmater.2c00601
Chem. Mater. 2022, 34, 5116−5124

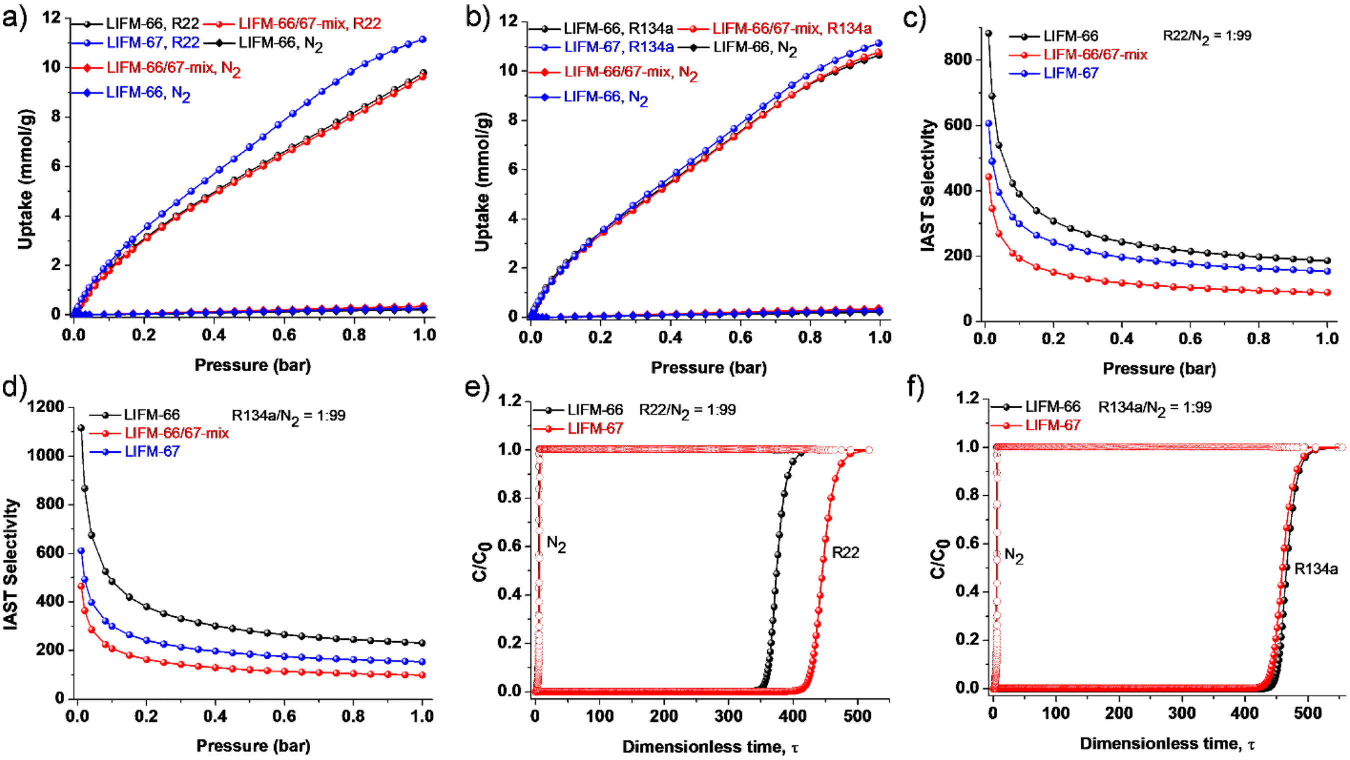

Figure 4. (a) R22 and N_2 adsorption isotherms at 298 K. (b) R134a and N_2 adsorption isotherms at 298 K. (c, d) IAST calculated selectivity of R22/N_2 (1:99) and R134a/N_2 (1:99) at 298 K. (e, f) Transient breakthrough simulations for the separation of R22/N_2 (1:99) and R134a/N_2 (1:99) mixtures using LIFM-66 and LIF-67 at 298 K with a total pressure of 101 kPa.

1.72 mol kg^{-1}, suggesting that LIFM-67 has better R22/N_2 isolation and concentration performance than LIFM-66. For R134a/N_2 separation, LIFM-66 and LIFM-67 present comparable performance with the calculated R134a capture capacity for 1:99 and 10:90 mixtures of R134a/N_2 to be 0.24 and 1.78 mol kg^{-1} by LIFM-66 and 0.23 and 1.74 mol kg^{-1} by LIFM-67. To evaluate the practical separation performance, we conducted the dynamic breakthrough experiments under 10 and 50% humid conditions, in which R134a/N_2 (1:99) gas mixtures flow over a fixed-bed column with a rate of 20 mL min^{-1}. As shown in Figures S57and S58, both LIFM-66/67 present excellent R134a separation potential with the R134a capture capacity of 0.31 (LIFM-66) and 0.42 (LIFM-67) mol kg^{-1} under 50% humid conditions. In the breakthrough process, N_2 elution appears immediately while R22 and R134a elute several hundred seconds later, which suggests effective isolation and concentration of R22 and R134a from the N_2 atmosphere for a practical detection and sequestration purpose under ordinary conditions, indicating potential to use these mixed-ligand MOFs as filling absorbents to harvest the trace Freon gases for analysis.

Because the kinetics of R22 and R134a adsorption play a crucial role in evaluating their practical detection and industry applications besides other performance characteristics including stability, capacity, and selectivity, the adsorption kinetic experiments are conducted at 298 K and 0.95 bar. As depicted in Figure 5, these mixed-ligand MOFs exhibit rapid adsorption kinetics for R22 and R134a. The complete adsorption saturation can be achieved in just 26 (R22) or 36 (R134a) minutes, justifying a fast uptake rate that facilitates a pressure-swing adsorption process. Moreover, the fast adsorption kinetics signify high diffusivity of adsorbates in MOF pores, benefiting the response rate of detection analysis. Therefore,

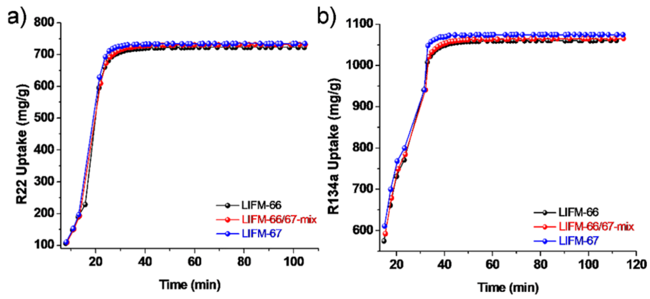

Figure 5. (a) R22 adsorption kinetic isotherms at 298 K and 0.95 bar. (b) R134a adsorption kinetic isotherms at 298 K and 0.95 bar.

this mixed-ligand MOF series successfully realizes a combination of excellent stability, ultrahigh R22 and R134a capture capacity, high R22/N_2 and R134a/N_2 selectivity, and fast adsorption kinetics, which is beneficial for the application processes such as capture, isolation, concentration, sequestration, and reclamation.

■ CONCLUSIONS

In summary, we have successfully constructed a series of microporous mixed-ligand MOFs, LIFM-66, 66/67-mix, and 67, by means of pore-nanospace engineering through incorporating different linkers of H_3BTB, H_3CTTA, and H_4ETTC with distinct molecular characters and functional groups. These mixed-ligand MOFs show a high BET surface area and good thermal and chemical stability. Noteworthily, they feature exceptional R22 and R134a adsorption capacity, high R22/N_2 and R134a/N_2 selectivity, and fast uptake kinetics, suggesting great potential for Freon gas capture, isolation, concentration, and sequestration under ordinary

https://doi.org/10.1021/acs.chemmater.2c00601
Chem. Mater. 2022, 34, 5116−5124

conditions. Moreover, the pore environment can be finely tuned by introducing methyl functionalized groups, which results in improved adsorption performance of R22, R134a, and CO_2 greenhouse gases. A synergistic effect contributed by the appropriate gas affinity and high pore surface area is elucidated for the low-pressure adsorption of Freon gases. These findings may offer a guideline for future design and fabrication of mixed-ligand MOFs by virtue of organic-linker variation and modification for gas adsorption-based applications.

■ ASSOCIATED CONTENT

Supporting Information

The Supporting Information is available free of charge at https://pubs.acs.org/doi/10.1021/acs.chemmater.2c00601.

Detailed experimental methods, characterization details, adsorption isotherms, simulated transient breakthrough, and modeling studies (PDF)

Crystallographic data for LIFM-67 (CIF)

■ AUTHOR INFORMATION

Corresponding Authors

Cheng-Xia Chen − *MOE Laboratory of Bioinorganic and Synthetic Chemistry, Lehn Institute of Functional Materials, School of Chemistry, Sun Yat-Sen University, Guangzhou 510275, China*; Email: chenchx29@mail.sysu.edu.cn

Mei Pan − *MOE Laboratory of Bioinorganic and Synthetic Chemistry, Lehn Institute of Functional Materials, School of Chemistry, Sun Yat-Sen University, Guangzhou 510275, China*; orcid.org/0000-0002-8979-7305; Email: panm@mail.sysu.edu.cn

Cheng-Yong Su − *MOE Laboratory of Bioinorganic and Synthetic Chemistry, Lehn Institute of Functional Materials, School of Chemistry, Sun Yat-Sen University, Guangzhou 510275, China; State Key Laboratory of Applied Organic Chemistry, Lanzhou University, Lanzhou 730000, China*; orcid.org/0000-0003-3604-7858; Email: cesscy@mail.sysu.edu.cn

Authors

Yang-Yang Xiong − *MOE Laboratory of Bioinorganic and Synthetic Chemistry, Lehn Institute of Functional Materials, School of Chemistry, Sun Yat-Sen University, Guangzhou 510275, China*

Rajamani Krishna − *Van't Hoff Institute for Molecular Sciences, University of Amsterdam, 1098 XH Amsterdam, The Netherlands*; orcid.org/0000-0002-4784-8530

Tony Pham − *Department of Chemistry, University of South Florida, Tampa, Florida 33620, United States*; orcid.org/0000-0001-5654-163X

Katherine A. Forrest − *Department of Chemistry, University of South Florida, Tampa, Florida 33620, United States*

Zhang-Wen Wei − *MOE Laboratory of Bioinorganic and Synthetic Chemistry, Lehn Institute of Functional Materials, School of Chemistry, Sun Yat-Sen University, Guangzhou 510275, China*; orcid.org/0000-0002-8378-2479

Ji-Jun Jiang − *MOE Laboratory of Bioinorganic and Synthetic Chemistry, Lehn Institute of Functional Materials, School of Chemistry, Sun Yat-Sen University, Guangzhou 510275, China*; orcid.org/0000-0001-9483-6033

Hai-Ping Wang − *School of Biotechnology and Health Sciences, Wuyi University, Jiangmen 529020, P. R. China*

Yanan Fan − *MOE Laboratory of Bioinorganic and Synthetic Chemistry, Lehn Institute of Functional Materials, School of Chemistry, Sun Yat-Sen University, Guangzhou 510275, China*

Complete contact information is available at: https://pubs.acs.org/10.1021/acs.chemmater.2c00601

Notes

The authors declare no competing financial interest.

■ ACKNOWLEDGMENTS

This work was supported by the NKRD Program of China (2021YFA1500401), the NSFC Projects (21890380, 21821003, 22090061, and 22001271), Chinese Postdoctoral Science Found (2017M622866), the International Postdoctoral Exchange Fellowship Program (20180055), and FRF for the Central Universities (20lgpy79). T.P. and K.A.F. acknowledge the use of services provided by Research Computing at the University of South Florida and High-Performance Computing at North Carolina State University.

■ REFERENCES

(1) Casper, J. K. *Greenhouse Gases: Worldwide Impacts*; Infobase Publishing, 2009; pp. 1−270.

(2) Solomon, S.; Qin, D.; Manning, M.; Chen, Z.; Marquis, M.; Averyt, K. B.; Tignor, M.; Miller, H. L., Eds; *Climate Change 2007: The Physical Science Basis, Contribution of working group I to the fourth assessment report of the intergovernmental panel on climate change*; Cambridge University Press, 2007.

(3) Kirsch, P. *Modern Fluoroorganic Chemistry: Synthesis, Reactivity, Applications*; Wiley-VCH publishing, 2013; pp. 1−108.

(4) Laube, J. C.; Newland, M. J.; Hogan, C.; Brenninkmeijer, C. A. M.; Fraser, P. J.; Martinerie, P.; Oram, D. E.; Reeves, C. E.; Röckmann, T.; Schwander, J.; Witrant, E.; Sturges, W. T. Newly detected ozone-depleting substances in the atmosphere. *Nat. Geosci.* **2014**, *7*, 266−269.

(5) Wang, D. C.; Li, Y. H.; Li, D.; Xia, Y. Z.; Zhang, J. P. A review on adsorption refrigeration technology and adsorption deterioration in physical adsorption systems. *Renew. Sustain. Energy Rev.* **2010**, *14*, 344−353.

(6) Ochoa-Herrera, V.; Sierra-Alvarez, R. Removal of perfluorinated surfactants by sorption onto granular activated carbon, zeolite and sludge. *Chemosphere* **2008**, *72*, 1588−1593.

(7) Lv, J.; Cheng, Y. Fluoropolymers in biomedical applications: state-of-the-art and future perspectives. *Chem. Soc. Rev.* **2021**, *50*, 5435−5467.

(8) Sicard, A. J.; Baker, R. T. Fluorocarbon Refrigerants and their Syntheses: Past to Present. *Chem. Rev.* **2020**, *120*, 9164−9303.

(9) Chen, T. H.; Popov, I.; Kaveevivitchai, W.; Chuang, Y. C.; Chen, Y. S.; Jacobson, A. J.; Miljanić, O. Š. Mesoporous fluorinated metal-organic frameworks with exceptional adsorption of fluorocarbons and CFCs. *Angew. Chem., Int. Ed.* **2015**, *54*, 13902−13906.

(10) Wanigarathna, D. K. J. A.; Gao, J.; Liu, B. Metal-organic frameworks for adsorption-based separation of fluorocompounds: a review. *Mater. Adv.* **2020**, *1*, 310−320.

(11) Motkuri, R. K.; Annapureddy, H. V. R.; Vijaykumar, M.; Schaef, H. T.; Martin, P. F.; McGrail, B. P.; Dang, L. X.; Krishna, R.; Thallapally, P. K. Fluorocarbon adsorption in hierarchical porous frameworks. *Nat. Commun.* **2014**, *5*, 4368.

(12) Wanigarathna, D. K. J. A.; Gao, J. J.; Takanami, T.; Zhang, Q. C.; Liu, B. Adsorption separation of R-22, R-32 and R-125 fluorocarbons using 4A molecular sieve zeolite. *ChemSelect* **2016**, *1*, 3718−3722.

(13) Bullister, J. L.; Weiss, R. F. Determination of $CC_{13}F$ and $CC_{12}F_2$ in seawater and air. *Deep-Sea Res. A* **1988**, *35*, 839−853.

(14) Bullister, J. L.; Wisegarver, D. P. The shipboard analysis of trace levels of sulfur hexafluoride, chlorofluorocarbon-11 and chlorofluorocarbon-12 in seawater. *Deep-Sea Res. I* **2008**, *55*, 1063−1074.
(15) Vollmer, M. K.; Weiss, R. F. Simultaneous determination of sulfur hexafluoride and three chlorofluorocarbons in water and air. *Mar. Chem.* **2002**, *78*, 137−148.
(16) Singh, G.; Lee, J.; Karakoti, A.; Bahadur, R.; Yi, J.; Zhao, D.; AlBahily, K.; Vinu, A. Emerging trends in porous materials for CO_2 capture and conversion. *Chem. Soc. Rev.* **2020**, *49*, 4360−4404.
(17) Wai, H. C.; Noor, M. M.; Ahmad, Z. A.; Jamaludin, S. B.; Mohd Ishak, M. A.; Jusoh, M. S. Sustainable porous materials for gas adsorption applications; a concise review. *Adv. Mater. Res.* **2013**, *795*, 96−101.
(18) Wang, H.; Lustig, W. P.; Li, J. Sensing and capture of toxic and hazardous gases and vapors by metal-organic frameworks. *Chem. Soc. Rev.* **2018**, *47*, 4729−4756.
(19) Ding, M.; Flaig, R. W.; Jiang, H. L.; Yaghi, O. M. Carbon capture and conversion using metal-organic frameworks and MOF-based materials. *Chem. Soc. Rev.* **2019**, *48*, 2783−2828.
(20) Yang, L.; Qian, S.; Wang, X.; Cui, X.; Chen, B.; Xing, H. Energy-efficient separation alternatives: metal−organic frameworks and membranes for hydrocarbon separation. *Chem. Soc. Rev.* **2020**, *49*, 5359−5406.
(21) Adil, K.; Belmabkhout, Y.; Pillai, R. S.; Cadiau, A.; Bhatt, P. M.; Assen, A. H.; Maurin, G.; Eddaoudi, M. Gas/vapour separation using ultra-microporous metal-organic frameworks: insights into the structure/separation relationship. *Chem. Soc. Rev.* **2017**, *46*, 3402−3430.
(22) Britt, D.; Furukawa, H.; Wang, B.; Glover, T. G.; Yaghi, O. M. Highly efficient separation of carbon dioxide by a metal-organic framework replete with open metal sites. *Proc. Nati. Acad. Sci. U. S. A.* **2009**, *106*, 20637−20640.
(23) Sumida, K.; Rogow, D. L.; Mason, J. A.; McDonald, T. M.; Bloch, E. D.; Herm, Z. R.; Bae, T. H.; Long, J. R. Carbon dioxide capture in metal-organic frameworks. *Chem. Rev.* **2012**, *112*, 724−781.
(24) He, H.; Sun, F.; Aguila, B.; Perman, J. A.; Ma, S.; Zhu, G. A bifunctional metal-organic framework featuring the combination of open metal sites and Lewis basic sites for selective gas adsorption and heterogeneous cascade catalysis. *J. Mater. Chem. A* **2016**, *4*, 15240−15246.
(25) Furukawa, H.; Ko, N.; Go, Y. B.; Aratani, N.; Choi, S. B.; Choi, E.; Yazaydin, A. Ö.; Snurr, R. Q.; O'Keeffe, M.; Kim, J.; Yaghi, O. M. Ultrahigh porosity in metal-organic frameworks. *Science* **2010**, *329*, 424−428.
(26) Chen, B.; Xiang, S.; Qian, G. Metal-organic frameworks with functional pores for recognition of small molecules. *Acc. Chem. Res.* **2010**, *43*, 1115−1124.
(27) Yuan, S.; Zou, L. F.; Qin, J. S.; Li, J. L.; Huang, L.; Feng, L. A.; Wang, X. A.; Bosch, M.; Alsalme, A.; Cagin, T.; Zhou, H. C. Construction of hierarchically porous metal-organic frameworks through linker labilization. *Nat. Commun.* **2017**, *8*, 15356.
(28) Tan, Y. X.; Wang, F.; Zhang, J. Design and synthesis of multifunctional metal−organic zeolites. *Chem. Soc. Rev.* **2018**, *47*, 2130−2144.
(29) Qin, J. S.; Yuan, S.; Wang, Q.; Alsalme, A.; Zhou, H. C. Mixed-linker strategy for the construction of multifunctional metal−organic frameworks. *J. Mater. Chem. A* **2017**, *5*, 4280−4291.
(30) Ji, Z.; Wang, H.; Canossa, S.; Wuttke, S.; Yaghi, O. M. Pore Chemistry of Metal−organic frameworks. *Adv. Funct. Mater.* **2020**, *30*, 2000238−2000261.
(31) Lin, R. B.; Li, T. Y.; Zhou, H. L.; He, C. T.; Zhang, J. P.; Chen, X. M. Tuning fluorocarbon adsorption in new isoreticular porous coordination frameworks for heat transformation applications. *Chem. Sci.* **2015**, *6*, 2516−2521.
(32) Mo, Z. W.; Zhou, H. L.; Zhou, D. D.; Lin, R. B.; Liao, P. Q.; He, C. T.; Zhang, W. X.; Chen, X. M.; Zhang, J. P. Mesoporous metal-organic frameworks with exceptionally high working capacities for adsorption heat transformation. *Adv. Mater.* **2018**, *30*, No. 1704350.
(33) Zheng, J.; Barpaga, D.; Trump, B. A.; Shetty, M.; Fan, Y.; Bhattacharya, P.; Jenks, J. J.; Su, C. Y.; Brown, C. M.; Maurin, G.; McGrail, B. P.; Motkuri, R. K. Molecular insight into fluorocarbon adsorption in pore expanded metal-organic framework analogs. *J. Am. Chem. Soc.* **2020**, *142*, 3002−3012.
(34) Zheng, J.; Vemuri, R. S.; Estevez, L.; Koech, P. K.; Varga, T.; Camaioni, D. M.; Blake, T. A.; McGrail, B. P.; Motkuri, R. K. Pore-engineered metal-organic frameworks with excellent adsorption of water and fluorocarbon refrigerant for cooling applications. *J. Am. Chem. Soc.* **2017**, *139*, 10601−10604.
(35) Zheng, J.; Wahiduzzaman, M.; Barpaga, D.; Trump, B. A.; Gutiérrez, O. Y.; Thallapally, P.; Ma, S.; McGrail, B. P.; Maurin, G.; Motkuri, R. K. Porous covalent organic polymers for efficient fluorocarbon-based adsorption cooling. *Angew. Chem., Int. Ed.* **2021**, *60*, 18037−18043.
(36) Zheng, J.; Barpaga, D.; Gutiérrez, O. Y.; Browning, N. D.; Mehdi, B. L.; Farha, O. K.; Lercher, J. A.; McGrail, B. P.; Motkuri, R. K. Exceptional fluorocarbon uptake with mesoporous metal−organic frameworks for adsorption-based cooling systems. *ACS Appl. Energy Mater.* **2018**, *1*, 5853−5858.
(37) Chen, T.-H.; Popov, I.; Kaveevivitchai, W.; Chuang, Y.-C.; Chen, Y.-S.; Daugulis, O.; Jacobson, A. J.; Miljanić, O. Š. Thermally robust and porous noncovalent organic framework with high affinity for fluorocarbons and CFCs. *Nat. Commun.* **2014**, *5*, 5131.
(38) Yang, C.; Wang, X. P.; Omary, M. A. Fluorous Metal−Organic Frameworks for High-Density Gas Adsorption. *J. Am. Chem. Soc.* **2007**, *129*, 15454−15455.
(39) Chen, C. X.; Qiu, Q. F.; Cao, C. C.; Pan, M.; Wang, H. P.; Jiang, J. J.; Wei, Z. W.; Zhu, K.; Li, G. Q.; Su, C. Y. Stepwise engineering of pore environments and enhancement of CO_2/R22 adsorption capacity through dynamic spacer installation and functionality modification. *Chem. Commun.* **2017**, *53*, 11403−11406.
(40) Chen, C. X.; Zheng, S. P.; Wei, Z. W.; Cao, C. C.; Wang, H. P.; Wang, D. W.; Jiang, J. J.; Fenske, D.; Su, C. Y. A Robust metal-organic framework combining open metal sites and polar groups for methane purification and CO_2/fluorocarbon capture. *Chem. − Eur. J.* **2017**, *23*, 4060−4064.
(41) Ji, Z.; Li, T.; Yaghi, O. M. Sequencing of metals in mixed-ligand metal-organic frameworks. *Science* **2020**, *369*, 674−680.
(42) Helal, A.; Yamani, Z. H.; Cordova, K. E.; Yaghi, O. M. Mixed-ligand metal-organic frameworks. *Natl. Sci. Rev.* **2017**, *4*, 296−298.
(43) Deng, H.; Doonan, C. J.; Furukawa, H.; Ferreira, R. B.; Towne, J.; Knobler, C. B.; Wang, B.; Yaghi, O. M. Multiple functional groups of varying ratios in metal-organic frameworks. *Science* **2010**, *327*, 846−850.
(44) Yuan, S.; Lu, W.; Chen, Y. P.; Zhang, Q.; Liu, T. F.; Feng, D.; Wang, X.; Qin, J.; Zhou, H. C. Sequential linker installation: precise placement of functional groups in mixed-ligand metal-organic frameworks. *J. Am. Chem. Soc.* **2015**, *137*, 3177−3180.
(45) Feng, L.; Wang, K. Y.; Day, G. S.; Zhou, H. C. The chemistry of multi-component and hierarchical framework compounds. *Chem. Soc. Rev.* **2019**, *48*, 4823−4853.
(46) Dong, Z.; Sun, Y.; Chu, J.; Zhang, X.; Deng, H. Mixed-ligand metal-organic frameworks for dialing-in the binding and programming the release of drug molecules. *J. Am. Chem. Soc.* **2017**, *139*, 14209−14216.
(47) Xia, Q.; Li, Z.; Tan, C.; Liu, Y.; Gong, W.; Cui, Y. Mixed-ligand metal-organic frameworks as multifunctional heterogeneous asymmetric catalysts for sequential reactions. *J. Am. Chem. Soc.* **2017**, *139*, 8259−8266.
(48) Chen, C. X.; Wei, Z. W.; Jiang, J. J.; Zheng, S. P.; Wang, H. P.; Qiu, Q. F.; Cao, C. C.; Fenske, D.; Su, C. Y. Dynamic spacer installation for multirole metal-organic frameworks: a new direction toward multifunctional MOFs achieving ultrahigh methane storage working capacity. *J. Am. Chem. Soc.* **2017**, *139*, 6034−6037.
(49) Wang, Y.; Feng, L.; Fan, W.; Wang, K. Y.; Wang, X.; Wang, X.; Zhang, K.; Zhang, X.; Dai, F.; Sun, D.; Zhou, H. C. Topology exploration in highly connected rare-earth metal-organic frameworks

https://doi.org/10.1021/acs.chemmater.2c00601
Chem. Mater. 2022, 34, 5116−5124

via continuous hindrance control. *J. Am. Chem. Soc.* **2019**, *141*, 6967−6975.
(50) Yuan, S.; Qin, J. S.; Zou, L.; Chen, Y. P.; Wang, X.; Zhang, Q.; Zhou, H. C. Thermodynamically guided synthesis of mixed-linker Zr-MOFs with enhanced tunability. *J. Am. Chem. Soc.* **2016**, *138*, 6636−6642.
(51) Chen, C. X.; Wei, Z.; Jiang, J. J.; Fan, Y. Z.; Zheng, S. P.; Cao, C. C.; Li, Y. H.; Fenske, D.; Su, C.-Y. Precise modulation of the breathing behavior and pore surface in Zr-MOFs by reversible post-synthetic variable-spacer installation to fine-tune the expansion magnitude and sorption properties. *Angew. Chem., Int. Ed.* **2016**, *55*, 9932−9936.
(52) Chen, C. X.; Wei, Z. W.; Fan, Y. N.; Su, P. Y.; Ai, Y. Y.; Qiu, Q. F.; Wu, K.; Yin, S. Y.; Pan, M.; Su, C. Y. Visualization of anisotropic and stepwise piezofluorochromism in an MOF single crystal. *Chem* **2018**, *4*, 2658−2669.
(53) Marsh, E. N. G. Fluorinated proteins: from design and synthesis to structure and stability. *Acc. Chem. Res.* **2014**, *47*, 2878−2886.
(54) Saha, B. B.; Habib, K.; El-Sharkawy, I. I.; Koyama, S. Adsorption characteristics and heat of adsorption measurements of R-134a on activated carbon. *Int. J. Refrig.* **2009**, *32*, 1563−1569.
(55) Myers, A. L.; Prausnitz, J. M. Thermodynamics of mixed-gas adsorption. *AIChE J.* **1965**, *11*, 121−127.
(56) Dreisbach, F.; Staudt, R.; Keller, J. U. High pressure adsorption data of methane, nitrogen, carbon dioxide and their binary and ternary mixtures on activated carbon. *Adsorption* **1999**, *5*, 215−227.
(57) Krishna, R. The Maxwell-Stefan description of mixture diffusion in nanoporous crystalline materials. *Microporous Mesoporous Mater.* **2014**, *185*, 30−50.
(58) Krishna, R. Methodologies for evaluation of metal−organic frameworks in separation applications. *RSC Adv.* **2015**, *5*, 52269−52295.
(59) Senkovska, I.; Barea, E.; Navarro, J. A. R.; Kaskel, S. Adsorptive capturing and storing greenhouse gases such as sulfur hexafluoride and carbon tetrafluoride using metal-organic frameworks. *Microporous Mesoporous Mater.* **2012**, *156*, 115−120.

https://doi.org/10.1021/acs.chemmater.2c00601
Chem. Mater. 2022, 34, 5116−5124

Pore-nanospace engineering of mixed-ligand metal-organic frameworks for high adsorption of hydrofluorocarbon and hydrochlorofluorocarbon

Yang-Yang Xiong,[a] Rajamani Krishna,[e] Tony Pham,[d] Katherine A. Forrest,[d] Cheng-Xia Chen,[a]* Zhang-Wen Wei,[a] Ji-Jun Jiang,[a] Hai-Ping Wang,[c] Yanan Fan,[a] Mei Pan[a]* & Cheng-Yong Su[a,b]*

[a] *MOE Laboratory of Bioinorganic and Synthetic Chemistry, Lehn Institute of Functional materials, School of Chemistry, Sun Yat-Sen University, Guangzhou 510275, China*

[b] *State Key Laboratory of Applied Organic Chemistry Lanzhou University, Lanzhou 730000, China*

[c] *School of Biotechnology and Health Sciences, Wuyi University, Jiangmen 529020, P. R. China*

[d] *Department of Chemistry, University of South Florida 4202 E. Fowler Avenue, Tampa, Florida 33620, United States*

[e] *Van't Hoff Institute for Molecular Sciences, University of Amsterdam, Science Park 904, 1098 XH Amsterdam, The Netherlands*

Content

S1. Experimental Methods

All the reagents and solvents were purchased from commercial sources and directly used without further purification. H_3BTB was obtained from ENERGY CHEMICAL. Solid-state IR spectra were recorded using Nicolet/Nexus-670 FT-IR spectrometer in the region of 4000-400 cm^{-1} using KBr pellets. Single crystal X-ray diffraction data were collected on an Agilent Technologies SuperNova X-RAY diffractometer system equipped with a Cu sealed tube (λ = 1.54178) at 50 kV and 0.80 mA. Powder X-ray diffraction (PXRD) was carried out with a Rigaku SmartLab diffractometer (Bragg-Brentano geometry, Cu-$K\alpha1$ radiation, λ = 1.54056 Å). Thermogravimetric analyses (TGA) were performed on a NETZSCH TG209 system in nitrogen under 1 atm at a heating rate of 10 °C min^{-1}. Nuclear magnetic resonance (NMR) data were collected on a 400 MHz Nuclear Magnetic Resonance Spectrometer. Gas adsorption isotherms with pressures in the range of 0-1.0 bar were obtained by a volumetric method using a Quantachrome autosorb-iQ2-MP gas adsorption analyzer, using ultra-high purity N_2, CO_2, R22 and R134a gases. Adsorption kinetic isotherms with the pressure point of 0.95 bar were obtained by a gravimetric method using a multi-station gravimetric gas/vapor adsorption instrument (BSD-VVS), using high purity R22 and R134a gases.

S2. Ligand Synthesis

4', 4''', 4''''', 4'''''''-(ethene-1, 1, 2, 2-tetrayl)tetrakis(([1, 1'-biphenyl]-4-carboxylic acid)) (H_4ETTC) and 5'-(4-carboxyphenyl)-2',4',6'-trimethyl-[1,1':3'1''-terphenyl]-4,4'-dicarboxylic acid (H_3CTTA) were synthesized according to a previously reported literature.[1,2]

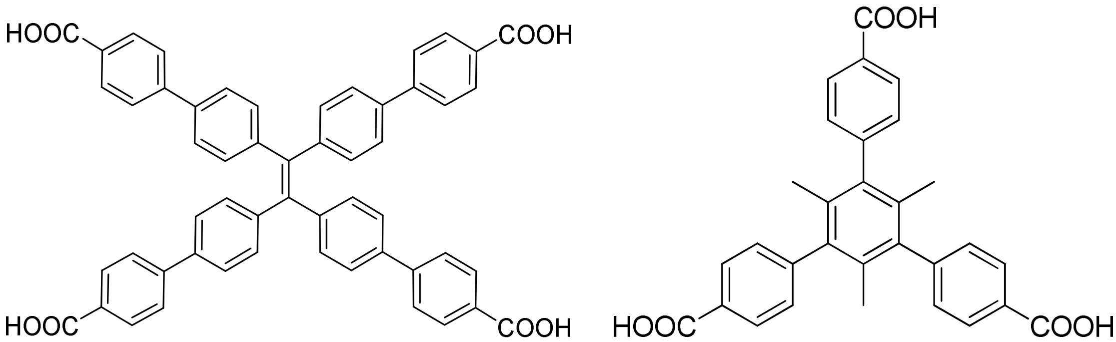

Scheme S1. Molecular structure of **H_4ETTC** (left) and **H_3CTTA** (right).

S3. Single Crystal X-Ray Crystallography

Single crystal of LIFM-67 was carefully picked and coated in paratone oil, attached to a glass silk which was inserted in a stainless steel stick, then quickly transferred to the Agilent Gemini S Ultra CCD Diffractometer with the Enhance X-ray Source of Cu radiation (λ = 1.54178 Å) using the ω-ϕ scan technique. All of the structures were solved by direct methods and refined by full-matrix least squares against F^2 using the SHELXL programs.[4] Hydrogen atoms were placed in geometrically calculated positions and included in the refinement process using riding model with isotropic thermal parameters: Uiso(H) = 1.2 Ueq(-CH). All the electrons of disordered solvent molecules which cannot be determined, are removed by SQUEEZE routine of PLATON program.[5] Crystal and refinement parameters are listed in Table S1.

Table S1. Crystallographic data for LIFM-67.

Compound	**LIFM-67**
CCDC	2114496
Formula	$C_{114}H_{74}O_{32}Zr_6$
Formula Weight	2502.85
Shape/Color	Hexagonal/Colorless
Crystal System	Hexagonal
Space Group	*P6/mmm*
T (K)	230(2)
a (Å)	20.2120(3)
b (Å)	20.2120(3)
c (Å)	21.9876(5)
α (°)	90.0
β (°)	90.0
γ (°)	120.0
V (Å3)	7779.1(3)
Z	2
D_{calc}(g/cm^3)	0.534
μ/mm^{-1}	1.823
F(000)	1254.0
R_1	0.0516
wR_2	0.1955
Completeness to theta	99.5 %
GOF	1.121

S4. ^{1}H NMR Spectrum

To digest the samples for ^{1}H NMR measurements, ~10 mg of samples were dissolved in 530 uL of 1.8 % D_2SO_4/DMSO-d_6.

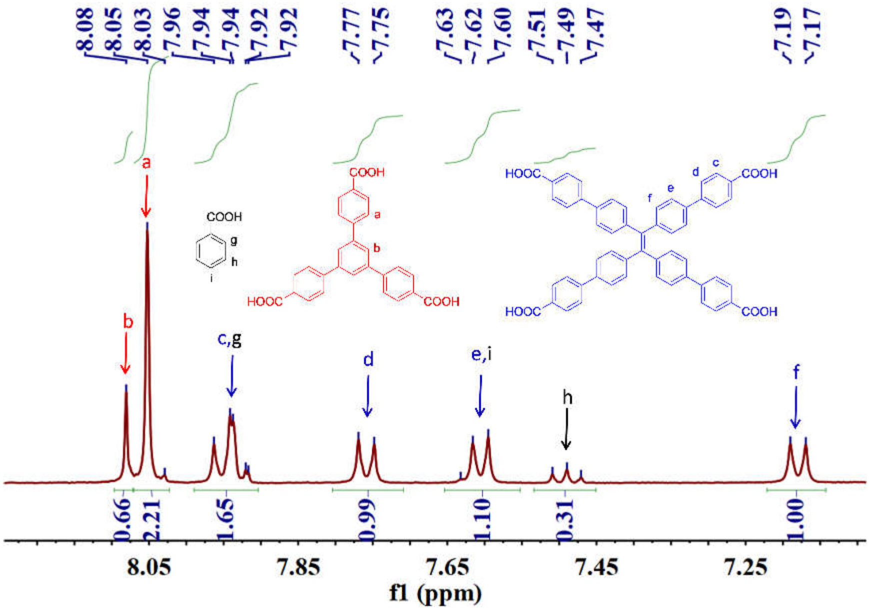

Figure S1. ^{1}H NMR spectroscopy of digested LIFM-66.

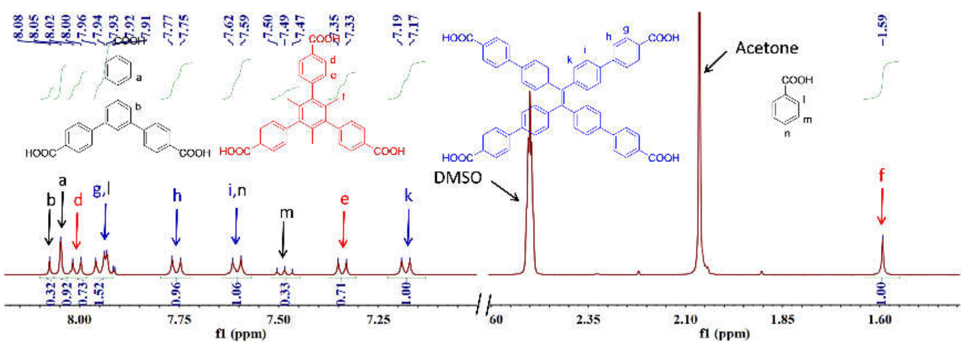

Figure S2. ^{1}H NMR spectroscopy of digested LIFM-66/67-mix.

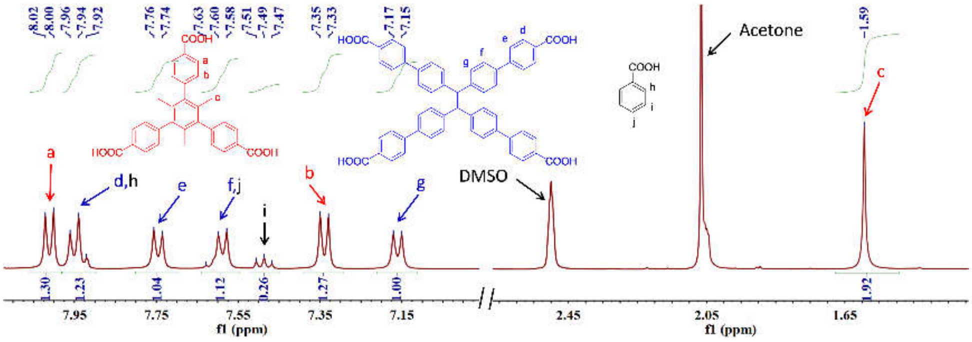

Figure S3. ^{1}H NMR spectroscopy of digested LIFM-67.

Table S2. Comparison of linker ratios from single crystal structure and from ^{1}H NMR of digested samples.

MOF	Linker ratios from crystal structure	Linker ratios from ^{1}H NMR of digested samples
LIFM-66	BTB : ETTC = 2:1	BTB : ETTC = ((2.21+0.66)/15) : (1.00/8) = 1.54:1
LIFM-66/67-mix	(BTB+CTTA) : ETTC = 2:1	(BTB+CTTA) : ETTC = ((0.92+0.32)/15+0.73/6) : (1.00/8) = (0.66+0.97) : 1 = 1.63:1
LIFM-67	CTTA : ETTC = 2:1	CTTA : ETTC = (1.3/6) : (1.00/8) = 1.73:1

S5. Scanning electron microscope (SEM) analysis

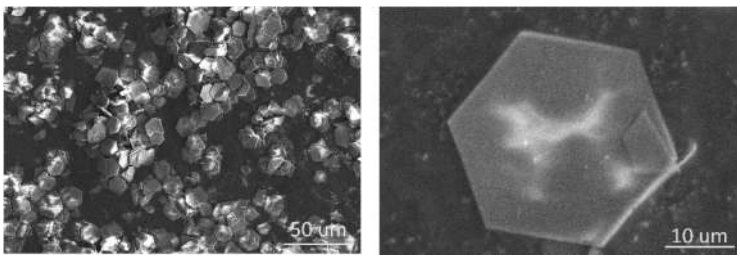

LIFM-66

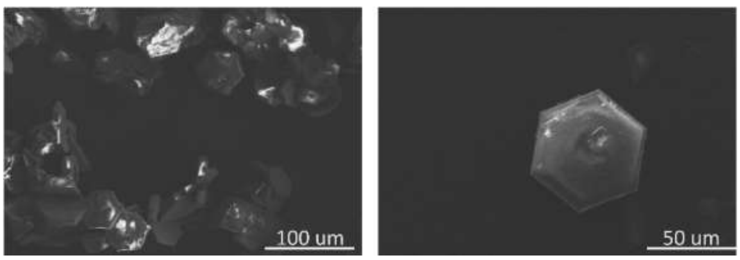

LIFM-66/67-mix

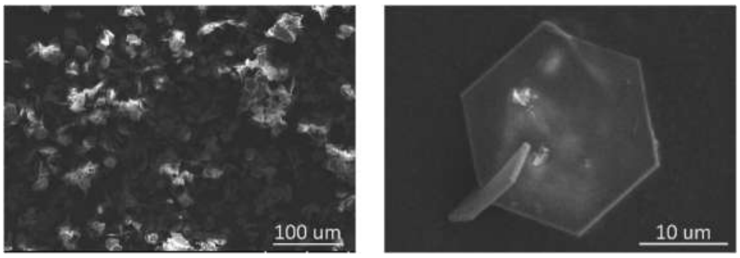

LIFM-67

Figure S4. The SEM images of LIFM-66, LIFM-66/67-mix and LIFM-67.

S6. Powder X-ray Diffraction (PXRD)

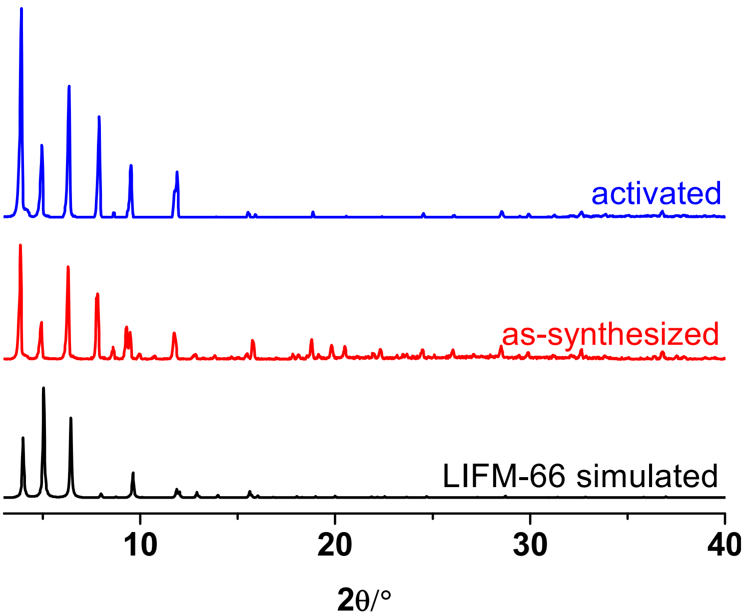

Figure S5. The PXRD patterns of LIFM-66.

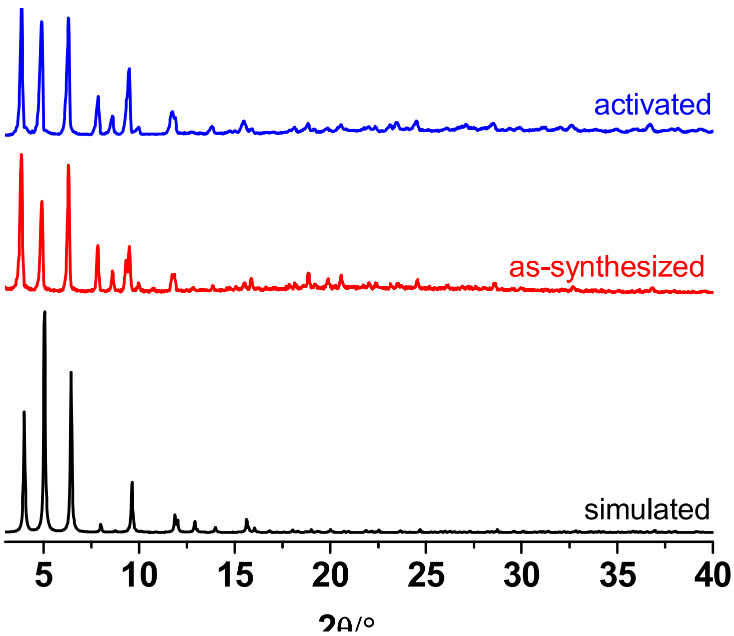

Figure S6. The PXRD patterns of LIFM-66/67-mix.

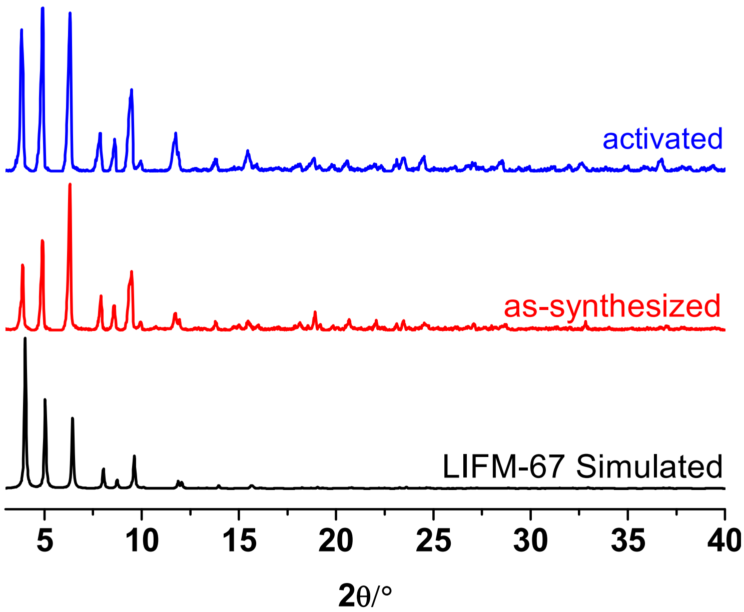

Figure S7. The PXRD patterns of LIFM-67.

S7. Thermogravimetric Analysis

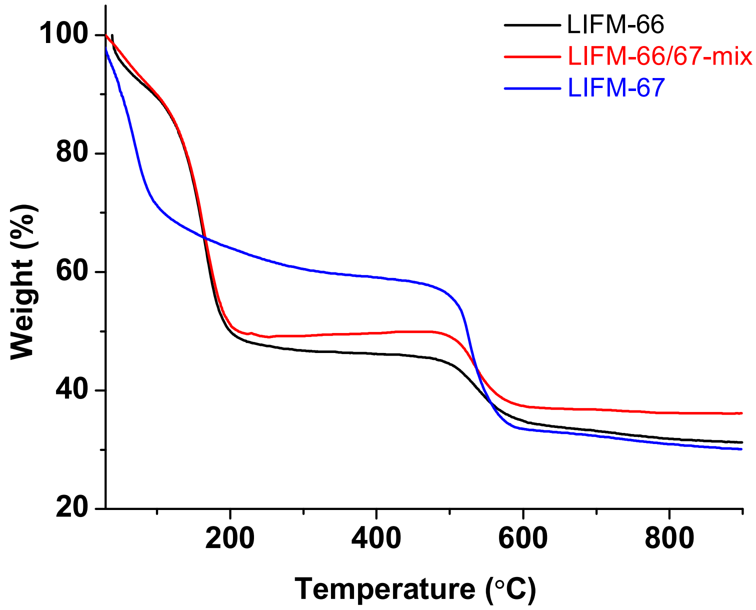

Figure S8. The thermogravimetric analysis of LIFM-66, LIFM-66/67-mix and LIFM-67.

S8. Porosity and Gas Adsorption Properties

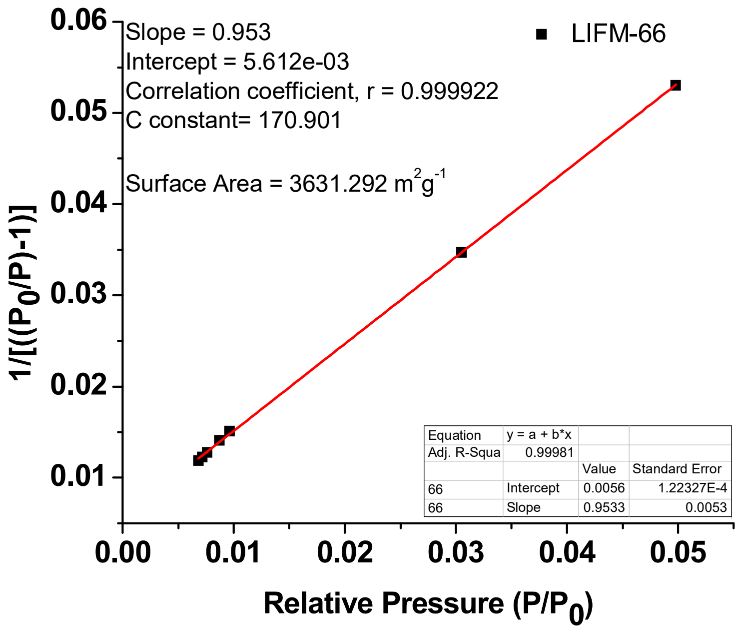

Figure S9. Plot of the linear region on the N_2 isotherm of LIFM-66 for the BET equation.

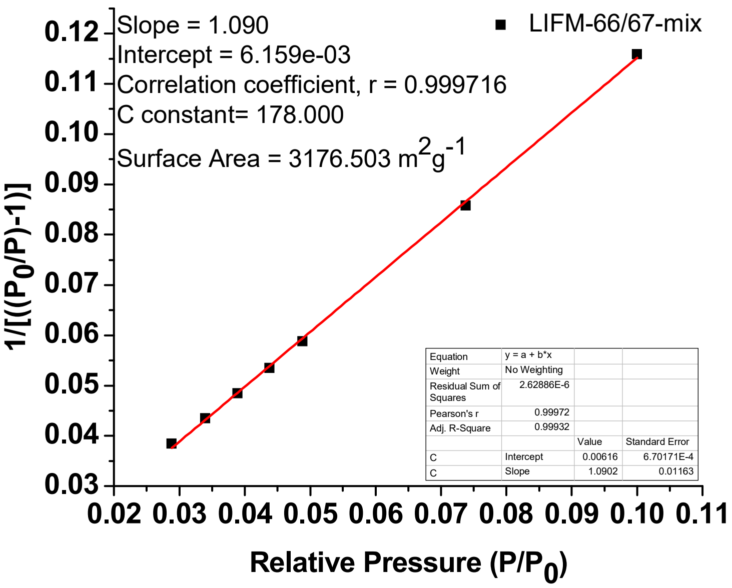

Figure S10. Plot of the linear region on the N_2 isotherm of LIFM-66/67-mix for the BET equation.

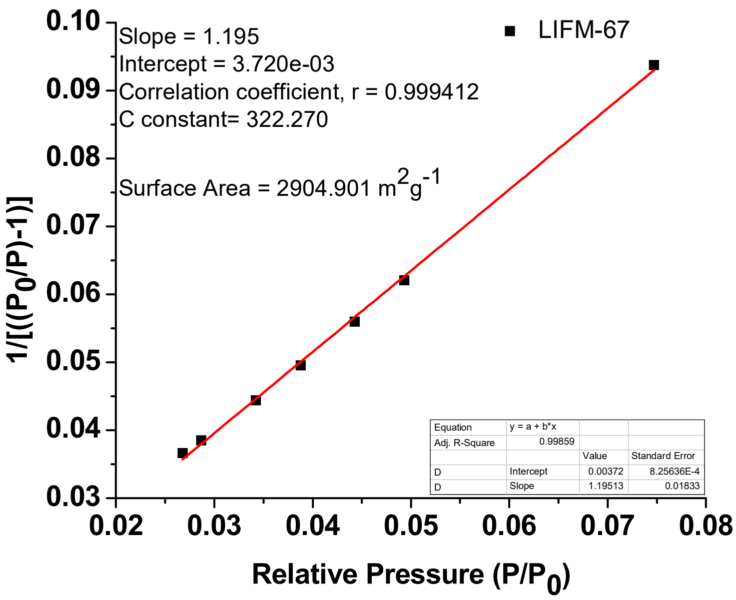

Figure S11. Plot of the linear region on the N_2 isotherm of LIFM-67 for the BET equation.

Table S3. The porosity parameters of LIFM-66, LIFM-66/67-MIX and LIFM-67.

Structure	S_{BET} (m^2/g)	Total Pore Volume (cc/g)	Pore Size by SF (Å)
LIFM-66	3631	1.42	16.2
LIFM-66/67-mix	3176	1.30	15.6
LIFM-67	2904	1.27	15.5

S9. Chemical Stability

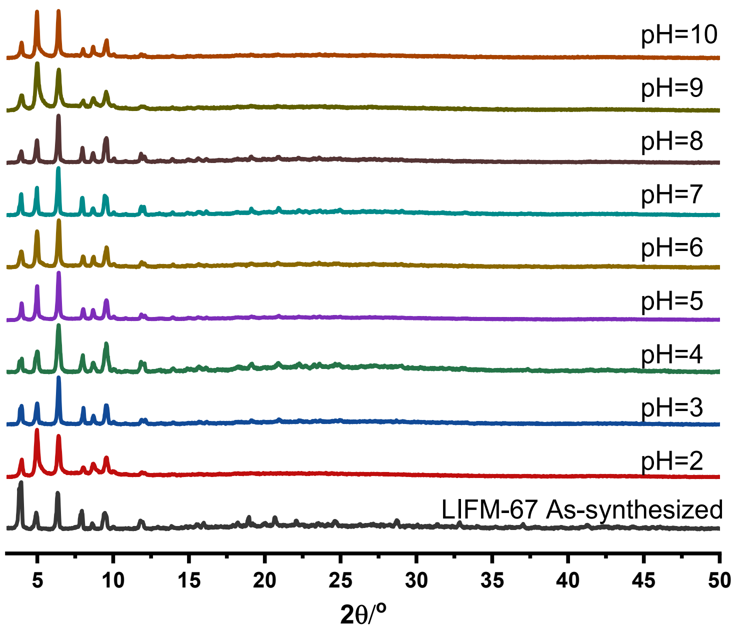

Figure S12. The PXRD patterns of LIFM-66/67-mix after immersing into aqueous solutions with different pH values for 48 h.

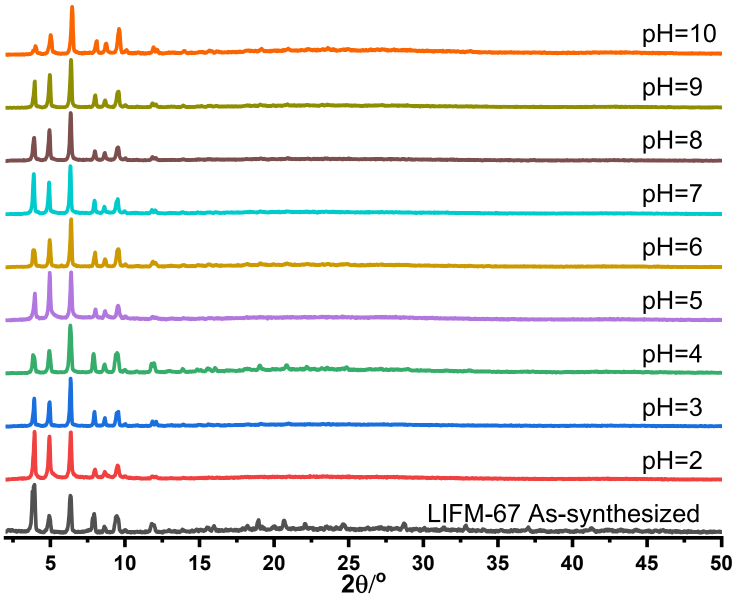

Figure S13. The PXRD patterns of LIFM-67 after immersing into aqueous solutions with different pH values for 48 h.

S10. R22, R134a and CO_2 Sorption Properties

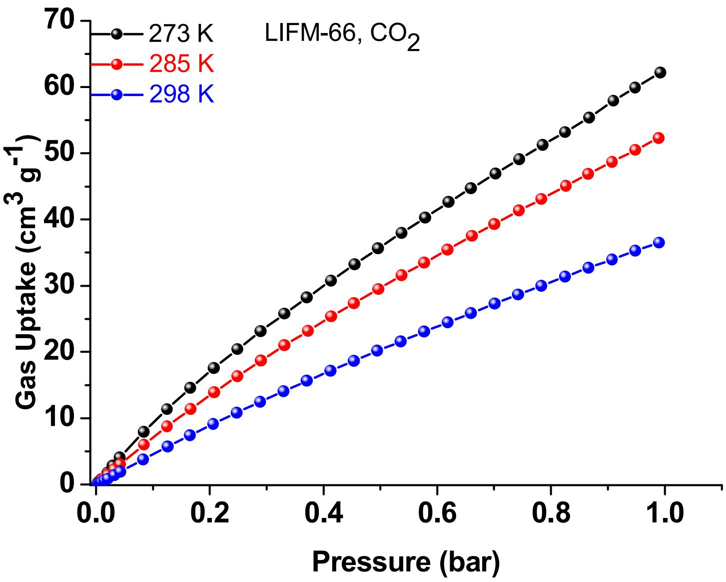

Figure S14. The CO_2 adsorption isotherms of LIFM-66 at 273 K, 285 K and 298 K.

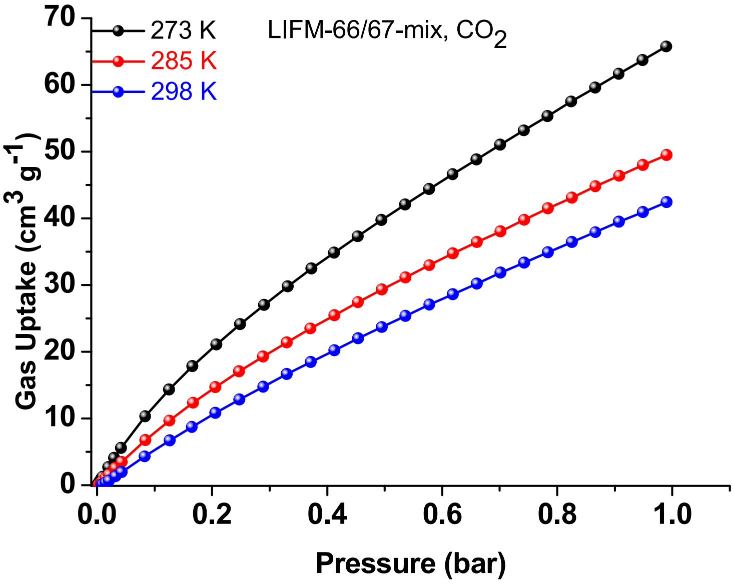

Figure S15. The CO_2 adsorption isotherms of LIFM-66/67-mix at 273 K, 285 K and 298 K.

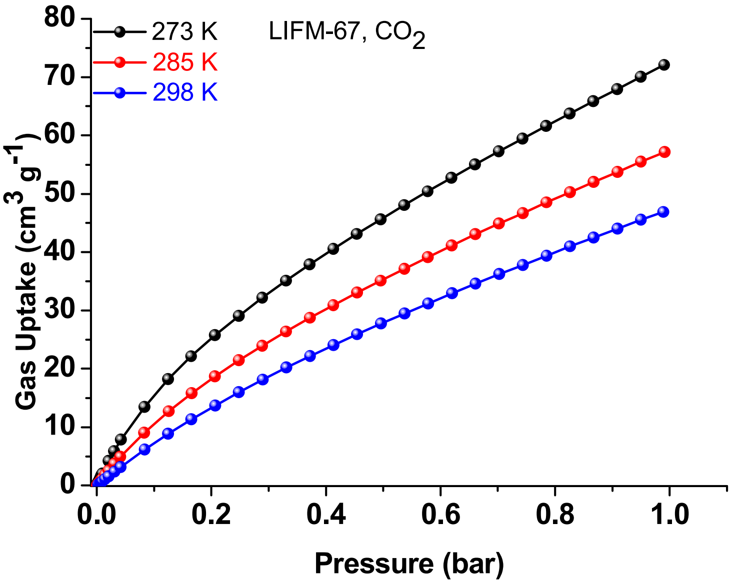

Figure S16. The CO_2 adsorption isotherms of LIFM-67 at 273 K, 285 K and 298 K.

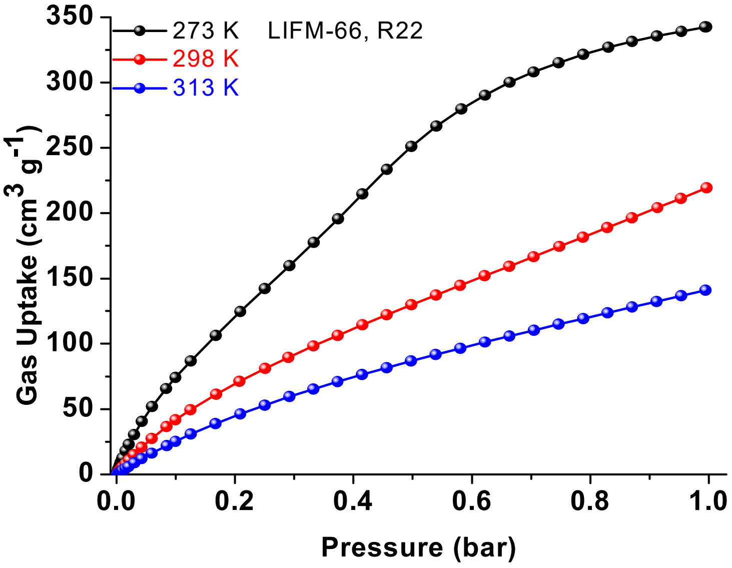

Figure S17. The R22 adsorption isotherms of LIFM-66 at 273 K, 298 K and 313 K.

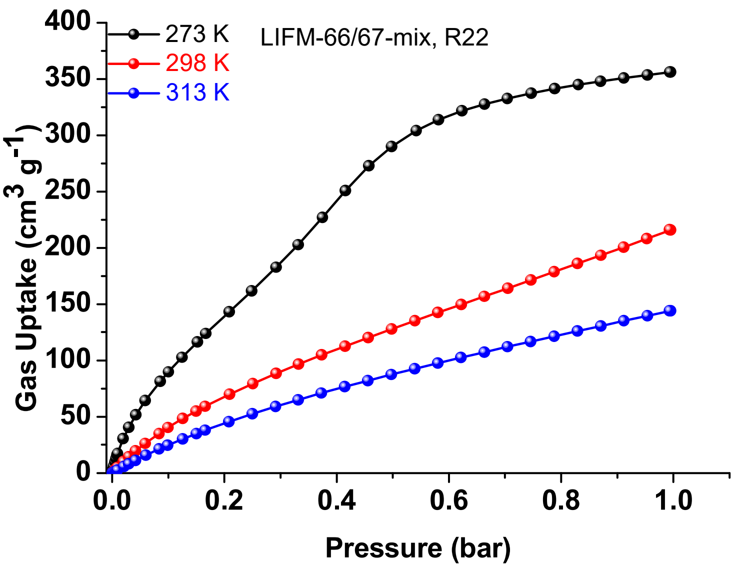

Figure S18. The R22 adsorption isotherms of LIFM-66/67-mix at 273 K, 298 K and 313 K.

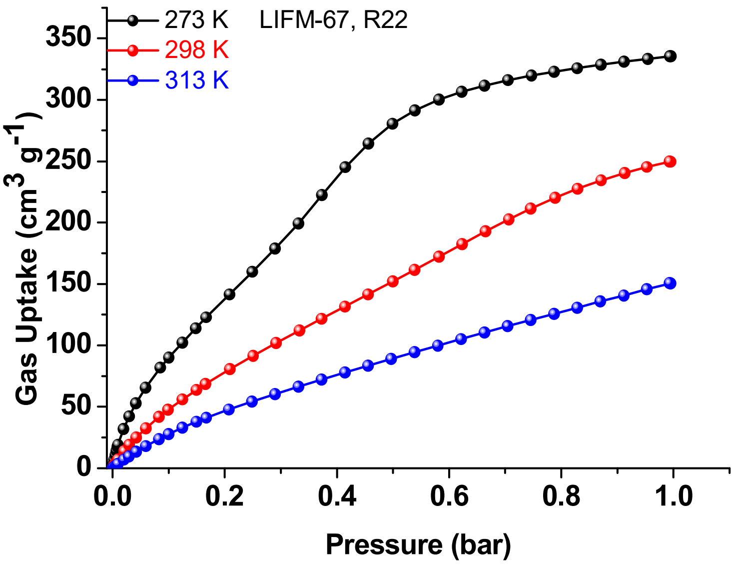

Figure S19. The R22 adsorption isotherms of LIFM-67 at 273 K, 298 K and 313 K.

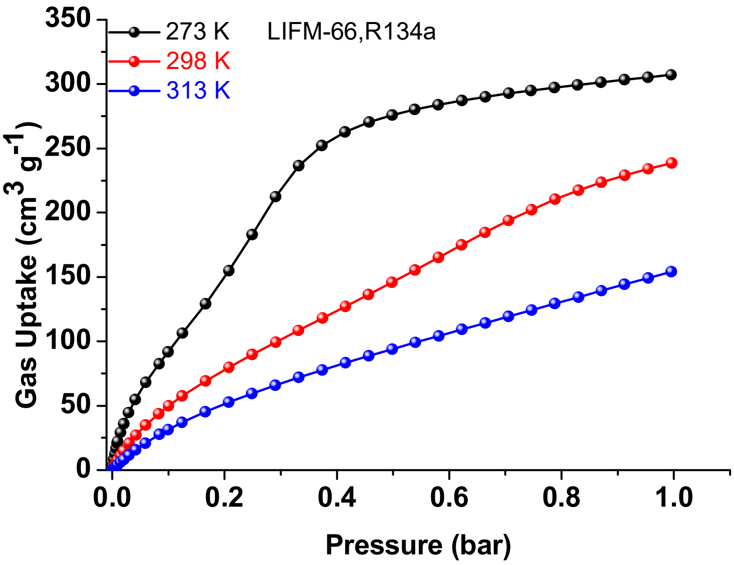

Figure S20. The R134a adsorption isotherms of LIFM-66 at 273 K, 298 K and 313 K.

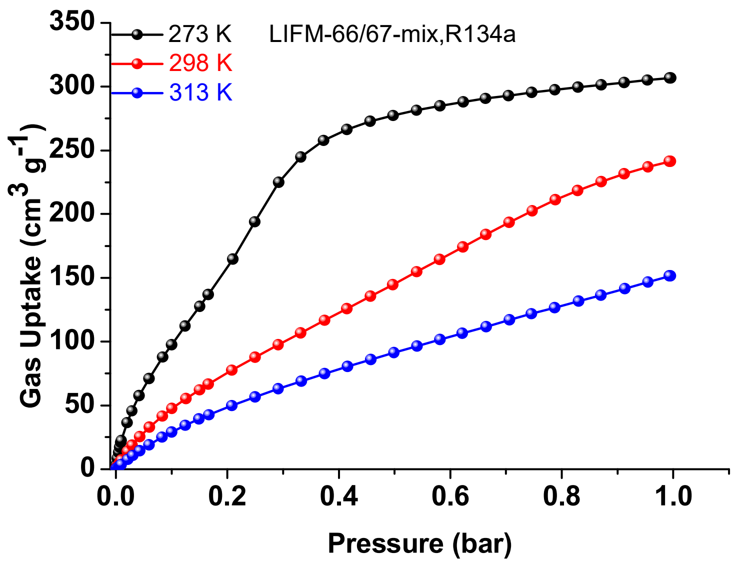

Figure S21. The R134a adsorption isotherms of LIFM-66/67-mix at 273 K, 298 K and 313 K.

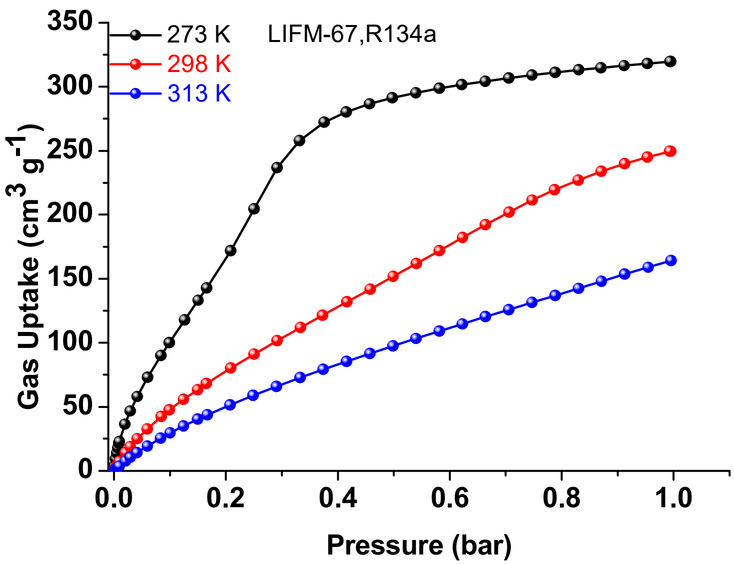

Figure S22. The R134a adsorption isotherms of LIFM-67 at 273 K, 298 K and 313 K.

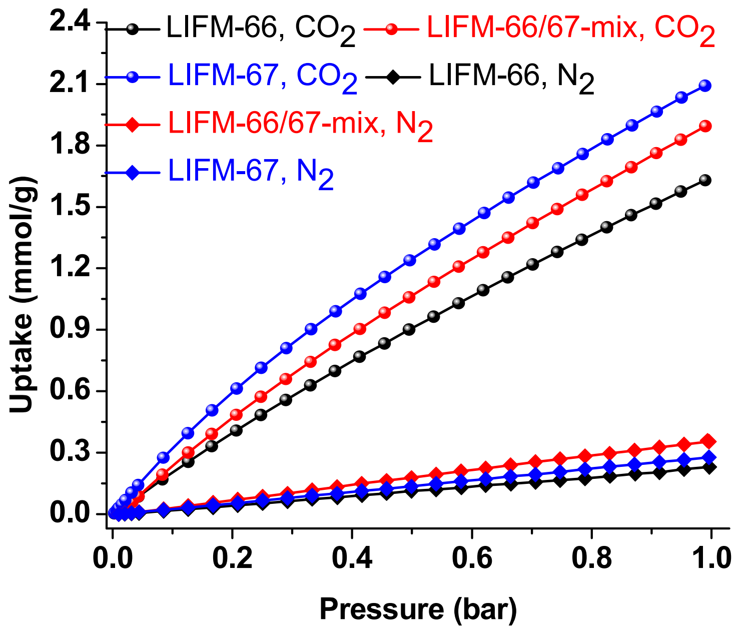

Figure S23. The CO_2 and N_2 adsorption isotherms of LIFM-66, 66/67-mix, and 67 at 298 K.

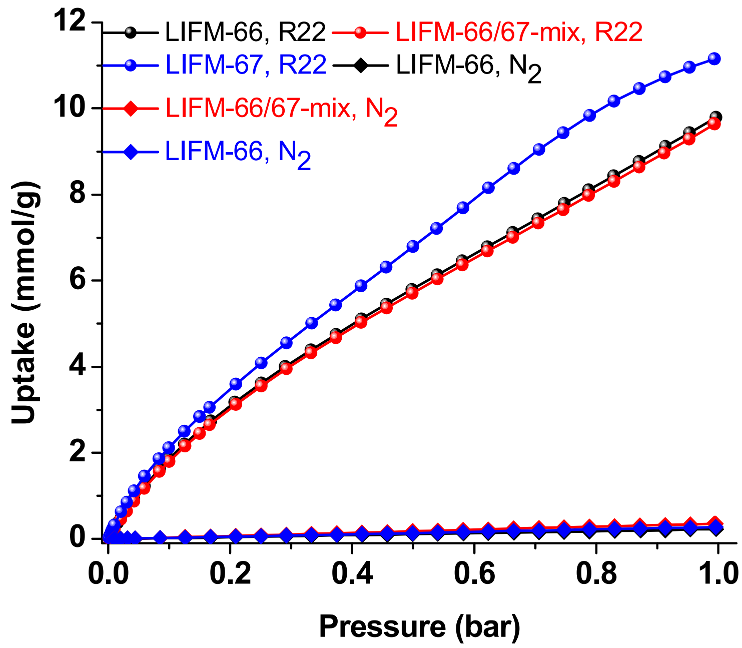

Figure S24. The R22 and N_2 adsorption isotherms of LIFM-66, 66/67-mix, and 67 at 298 K.

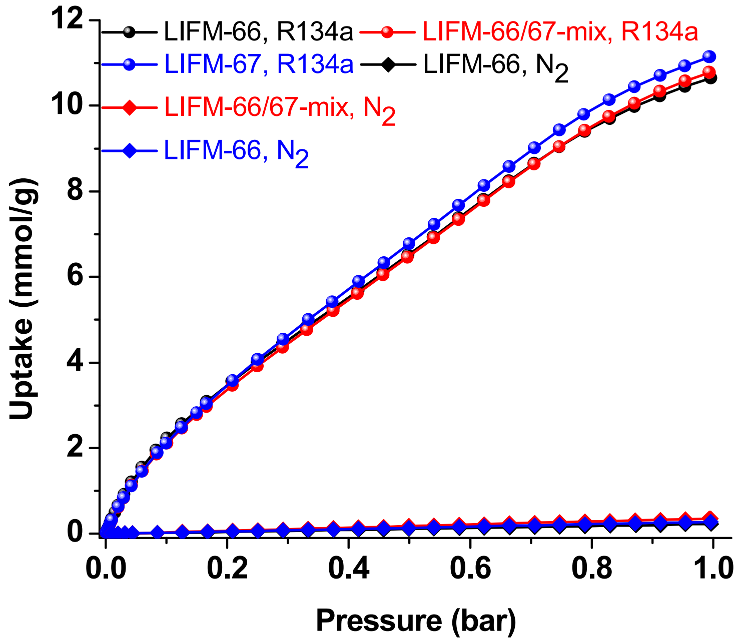

Figure S25. The R134a and N_2 adsorption isotherms of LIFM-66, 66/67-mix, and 67 at 298 K.

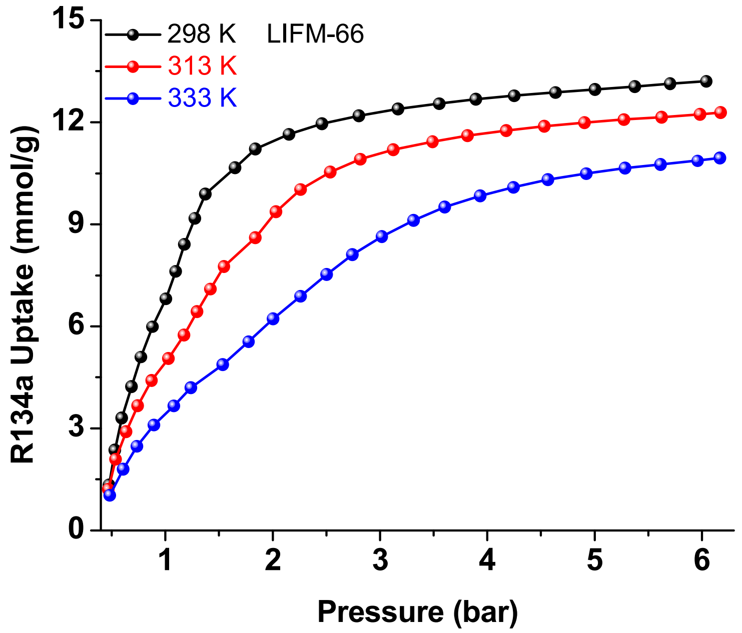

Figure S26. The R134a adsorption isotherms of LIFM-66 at 298, 313, and 333 K under high pressure.

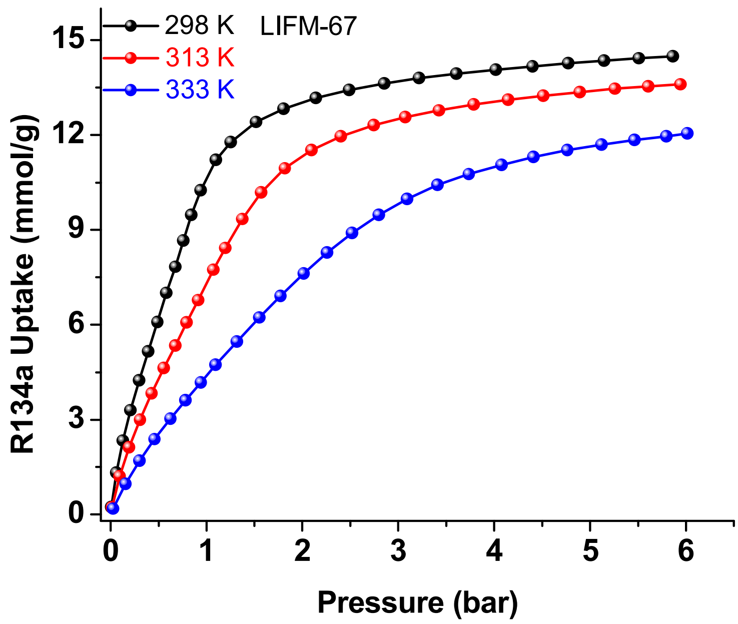

Figure S27. The R134a adsorption isotherms of LIFM-67 at 298, 313, and 333 K under high pressure.

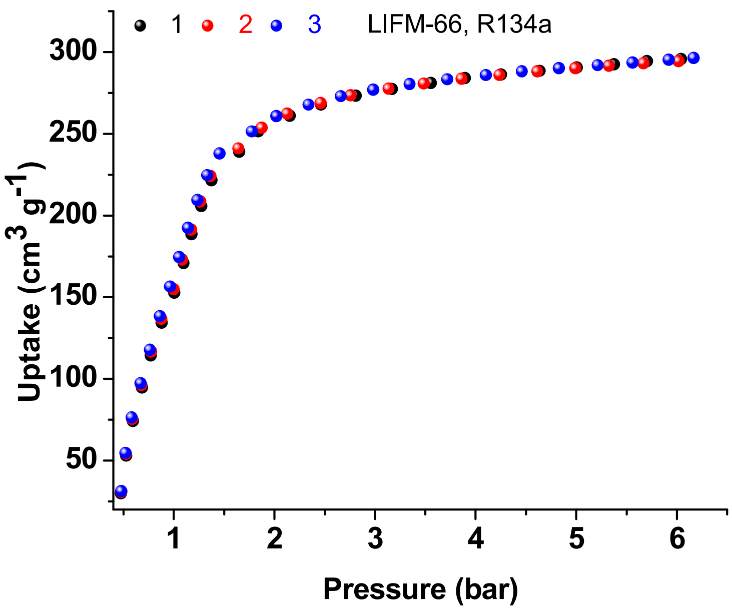

Figure S28. The continuous R134a adsorption isotherms of LIFM-66 at 298 K under high pressure.

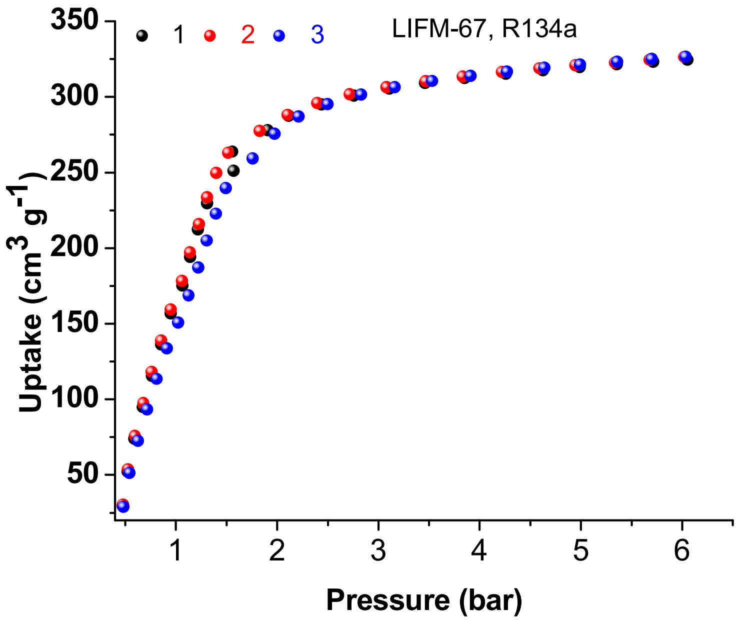

Figure S29. The continuous R134a adsorption isotherms of LIFM-67 at 298 K under high pressure.

Table S4. Comparison of R22 uptake performance at 298 K in reported MOFs.

Structure	BET Surface Area (m^2/g)	Pore Volume (cm^3/g)	Pore Size (Å)	R22 Uptake at 298 K, 1 bar (g/g)	Q_{st} (kJ/mol)	Source
LIFM-66	3631	1.42	16.2	0.85	27.9	This work
LIFM-66/67-MIX	3060	1.17	15.6	0.83	36.1	This work
LIFM-67	2904	1.27	15.5	0.96	36.2	This work
MIL-101	3450	1.66	11.7, 25, 29	0.85	34.6	6
MAF-X10	2032	0.80	7.2	0.82	32.8	7
MAF-X12	1787	0.72	6.6	0.73	31.8	7
MAF-X13	2742	1.07	9.4	0.97	31.4	7
LIFM-26	1513	0.59	12.6	0.56	25.0	8
LIFM-29	1247	0.63	13.2	0.52	27.0	9
LIFM-30	1176	0.67	12.7	0.54	36.5	9
LIFM-31	1410	0.74	13.3	0.61	26.7	9
LIFM-32	1472	0.69	13.2	0.43	33.6	9
LIFM-33	1588	0.76	12.7	0.32	33.9	9
LIFM-82	1624	0.71	12.7	0.76	31.3	10
LIFM-86	1269	0.60	12.7	0.54	30.4	10
LIFM-90	2222	0.92	13.2	0.86	33.1	11

Table S5. Comparison of R134a uptake performance at 298 K in reported MOFs.

Structure	BET Surface Area (m^2/g)	Pore Volume (cm^3/g)	Pore Size (Å)	R134a Uptake at 298 K, 1 bar (g/g)	Q_{st} (kJ/mol)	Source
LIFM-66	3631	1.42	16.2	1.09	35.6	This work
LIFM-66/67-MIX	3060	1.17	15.6	1.10	37.8	This work
LIFM-67	2904	1.27	15.5	1.14	38.9	This work
Ni-MOF-74	1150	0.51	11	0.53	50.6	12
Ni-TPP	1980	1.14	23	0.47	40.6	12
Ni-BPP	2040	0.89	17	0.60	44.2	12
Ni-BPM	2340	1.01	19	0.57	48.0	13
Ni-TPM	2420	1.49	27	0.65	45.0	13
MCF-61	2096	1.20	20	0.86	30.0	14
MCF-62	2630	1.98	33	0.77	29.3	14
MCF-63	2749	2.38	37	0.76	28.8	14
MOFF-5	2445	1.37	29.0, 34.1	0.55	---	15
PCN-222	169	1.24	12.6, 30.4	0.68	---	16

MIL-101	2642	1.88	11.7, 25, 29	0.78	---	16
NU-901	1864	1.38	11	0.85	---	16
NU-1000	2259	1.58	11.8, 29.5	0.80	32	16
COP-2	1783	1.76	---	0.63	24	17
COP-3	1835	1.64	---	0.67	24	17

S11. Calculations of Adsorption Isosteric Heats

The isosteric heats of CO_2, R22 and R134a adsorption for LIFM-66, LIFM-66/67-MIX, and LIFM-67 were calculated from the sorption data measured at 273, 285 and 298 K or at 273, 298 and 313 K by the virial fitting method, respectively. A virial-type expression (eq. 1) which is composed of parameters a_i and b_i is used. In eq. 1, P is the pressure in torr, N is the adsorbed amount in mmol·g^{-1}, T is the temperature in Kelvin, a_i and b_i are the virial coefficients which are independent of temperature, and m and n are the numbers of coefficients required to adequately describe the isotherms.

$$\ln P = \ln \mathrm{N} + \frac{1}{\mathrm{T}} \sum_{i=0}^{m} a_i \mathrm{N}^i + \sum_{i=0}^{n} b_i \mathrm{N}^i \qquad \text{eq. 1}$$

The values of the virial coefficients a_0 through a_m were then applied to calculate the isosteric heat of adsorption (eq 2). In eq. 2, Q_{st} is the coverage-dependent isosteric heat of adsorption, and *R* is the universal gas constant.[18]

$$\mathrm{Q_{st}} = -\mathrm{R} \sum_{i=0}^{m} a_i \mathrm{N}^i \qquad \text{eq. 2}$$

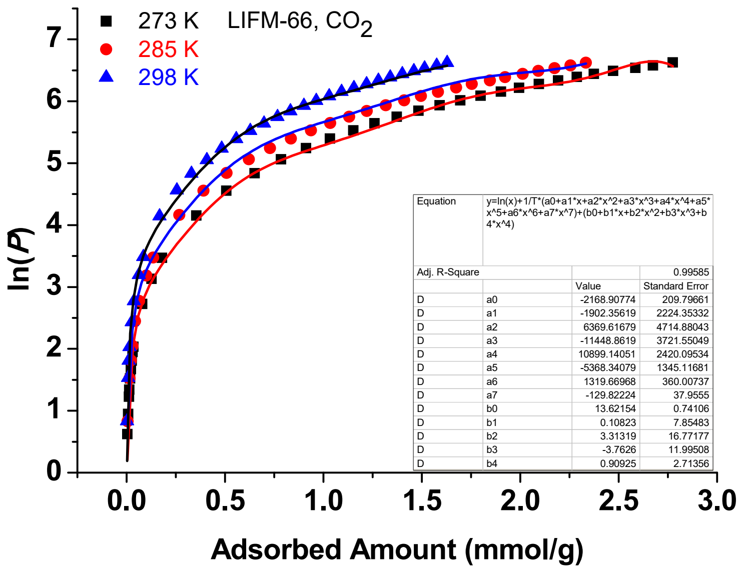

Equation	y=ln(x)+1/T*(a0+a1*x+a2*x^2+a3*x^3+a4*x^4+a5*x^5+a6*x^6+a7*x^7)+(b0+b1*x+b2*x^2+b3*x^3+b4*x^4)		
Adj. R-Square			0.99585
		Value	Standard Error
D	a0	-2168.90774	209.79661
D	a1	-1902.35619	2224.35332
D	a2	6369.61679	4714.88043
D	a3	-11448.8619	3721.55049
D	a4	10899.14051	2420.09534
D	a5	-5368.34079	1345.11681
D	a6	1319.66968	360.00737
D	a7	-129.82224	37.9555
D	b0	13.62154	0.74106
D	b1	0.10823	7.85483
D	b2	3.31319	16.77177
D	b3	-3.7626	11.99508
D	b4	0.90925	2.71356

Figure S30. CO_2 fitting (lines) of the adsorption isotherms (points) of LIFM-66 measured at 273, 285 and 298 K.

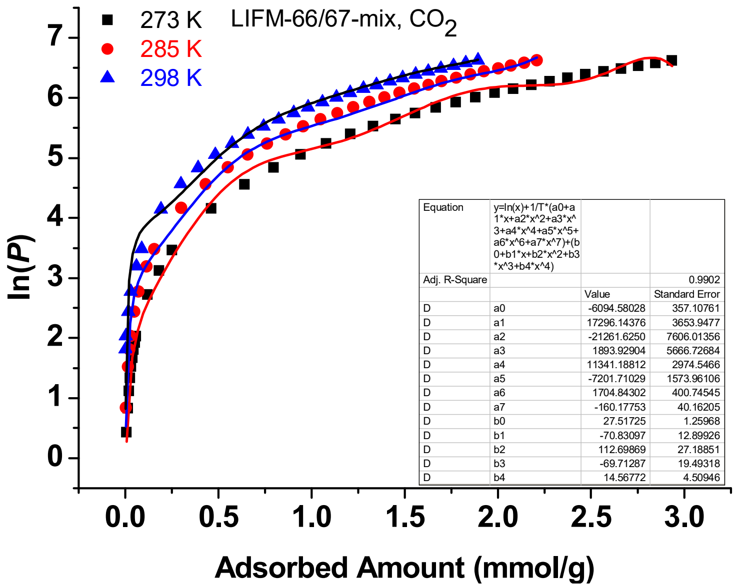

Equation	y=ln(x)+1/T*(a0+a1*x+a2*x^2+a3*x^3+a4*x^4+a5*x^5+a6*x^6+a7*x^7)+(b0+b1*x+b2*x^2+b3*x^3+b4*x^4)		
Adj. R-Square			0.9902
		Value	Standard Error
D	a0	-6094.58028	357.10761
D	a1	17296.14376	3653.9477
D	a2	-21261.6250	7606.01356
D	a3	1893.92904	5666.72684
D	a4	11341.18812	2974.5466
D	a5	-7201.71029	1573.96106
D	a6	1704.84302	400.74545
D	a7	-160.17753	40.16205
D	b0	27.51725	1.25968
D	b1	-70.83097	12.89926
D	b2	112.69869	27.18851
D	b3	-69.71287	19.49318
D	b4	14.56772	4.50946

Figure S31. CO_2 fitting (lines) of the adsorption isotherms (points) of LIFM-66/67-mix measured at 273, 285 and 298 K.

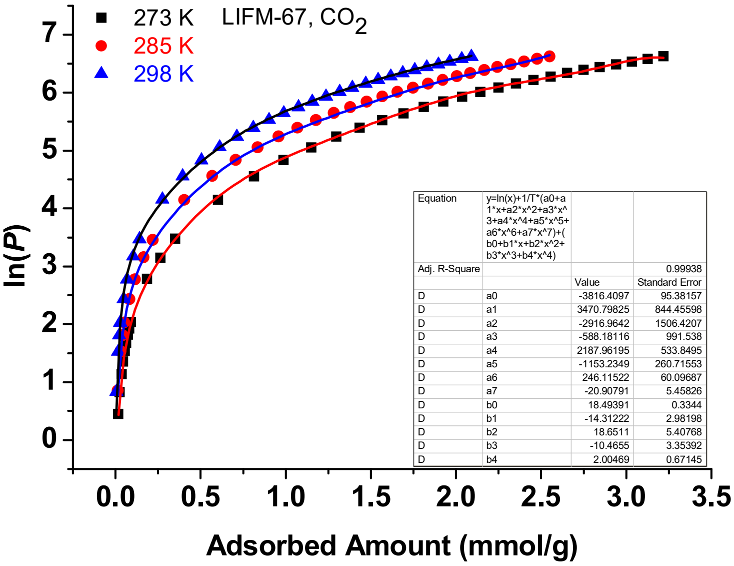

Equation	y=ln(x)+1/T*(a0+a1*x+a2*x^2+a3*x^3+a4*x^4+a5*x^5+a6*x^6+a7*x^7)+(b0+b1*x+b2*x^2+b3*x^3+b4*x^4)		
Adj. R-Square			0.99938
		Value	Standard Error
D	a0	-3816.4097	95.38157
D	a1	3470.79825	844.45598
D	a2	-2916.9642	1506.4207
D	a3	-588.18116	991.538
D	a4	2187.96195	533.8495
D	a5	-1153.2349	260.71553
D	a6	246.11522	60.09687
D	a7	-20.90791	5.45826
D	b0	18.49391	0.3344
D	b1	-14.31222	2.98198
D	b2	18.6511	5.40768
D	b3	-10.4655	3.35392
D	b4	2.00469	0.67145

Figure S32. CO_2 fitting (lines) of the adsorption isotherms (points) of LIFM-67 measured at 273, 285 and 298 K.

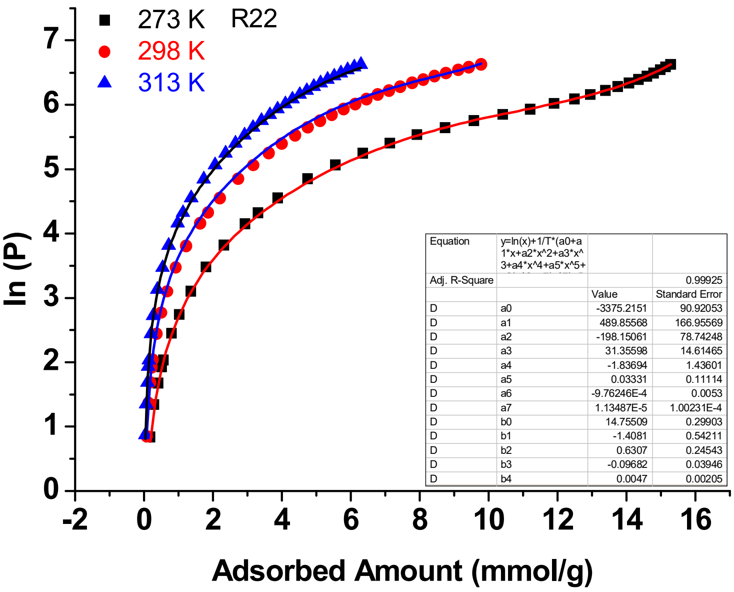

Equation	y=ln(x)+1/T*(a0+a1*x+a2*x^2+a3*x^3+a4*x^4+a5*x^5+		
Adj. R-Square			0.99925
		Value	Standard Error
D	a0	-3375.2151	90.92053
D	a1	489.85568	166.95569
D	a2	-198.15061	78.74248
D	a3	31.35598	14.61465
D	a4	-1.83694	1.43601
D	a5	0.03331	0.11114
D	a6	-9.76246E-4	0.0053
D	a7	1.13487E-5	1.00231E-4
D	b0	14.75509	0.29903
D	b1	-1.4081	0.54211
D	b2	0.6307	0.24543
D	b3	-0.09682	0.03946
D	b4	0.0047	0.00205

Figure S33. R22 fitting (lines) of the adsorption isotherms (points) of LIFM-66 measured at 273, 298 and 313 K.

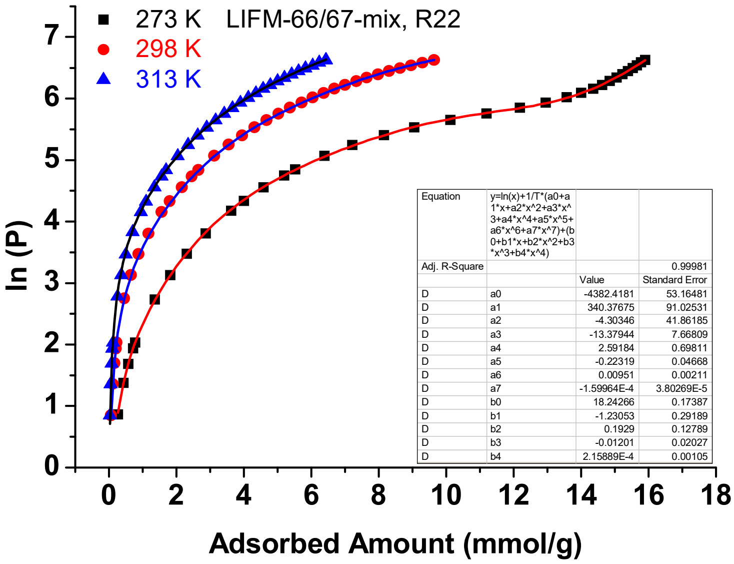

Equation	y=ln(x)+1/T*(a0+a1*x+a2*x^2+a3*x^3+a4*x^4+a5*x^5+a6*x^6+a7*x^7)+(b0+b1*x+b2*x^2+b3*x^3+b4*x^4)		
Adj. R-Square			0.99981
		Value	Standard Error
D	a0	-4382.4181	53.16481
D	a1	340.37675	91.02531
D	a2	-4.30346	41.86185
D	a3	-13.37944	7.66809
D	a4	2.59184	0.69811
D	a5	-0.22319	0.04668
D	a6	0.00951	0.00211
D	a7	-1.59964E-4	3.80269E-5
D	b0	18.24266	0.17387
D	b1	-1.23053	0.29189
D	b2	0.1929	0.12789
D	b3	-0.01201	0.02027
D	b4	2.15889E-4	0.00105

Figure S34. R22 fitting (lines) of the adsorption isotherms (points) of LIFM-66/67-mix measured at 273, 298 and 313 K.

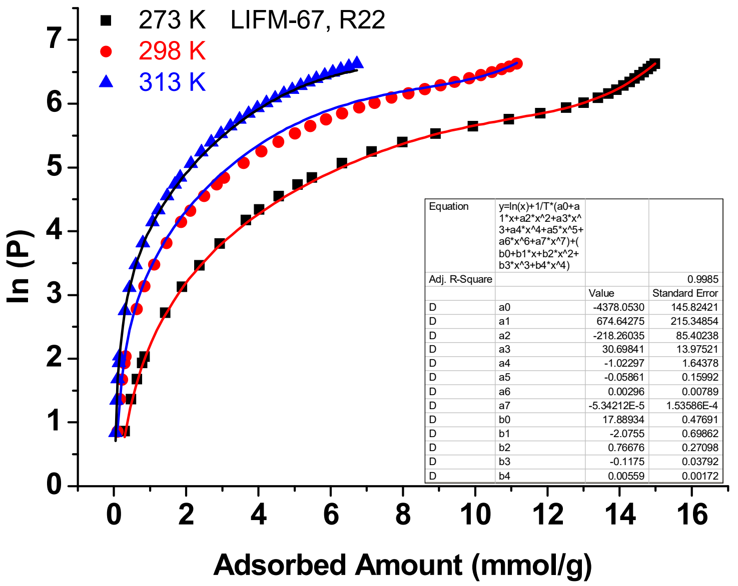

Equation	y=ln(x)+1/T*(a0+a1*x+a2*x^2+a3*x^3+a4*x^4+a5*x^5+a6*x^6+a7*x^7)+(b0+b1*x+b2*x^2+b3*x^3+b4*x^4)		
Adj. R-Square			0.9985
		Value	Standard Error
D	a0	-4378.0530	145.82421
D	a1	674.64275	215.34854
D	a2	-218.26035	85.40238
D	a3	30.69841	13.97521
D	a4	-1.02297	1.64378
D	a5	-0.05861	0.15992
D	a6	0.00296	0.00789
D	a7	-5.34212E-5	1.53586E-4
D	b0	17.88934	0.47691
D	b1	-2.0755	0.69862
D	b2	0.76676	0.27098
D	b3	-0.1175	0.03792
D	b4	0.00559	0.00172

Figure S35. R22 fitting (lines) of the adsorption isotherms (points) of LIFM-67 measured at 273, 298 and 313 K.

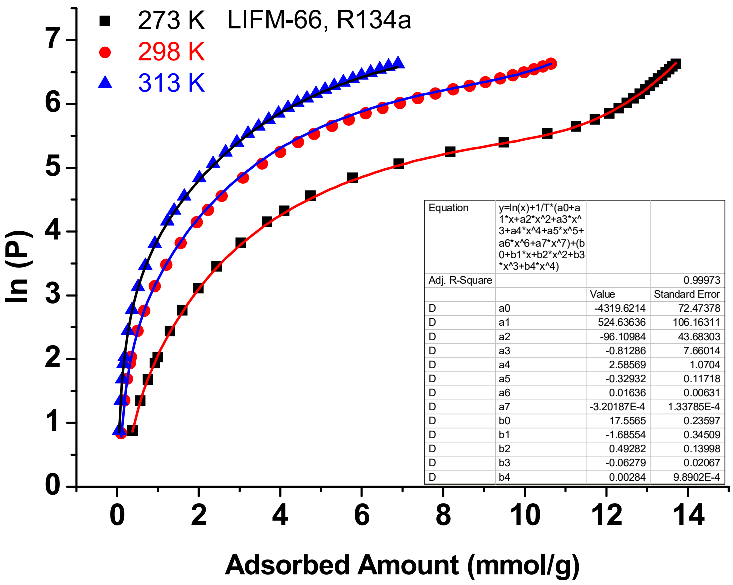

Figure S36. R134a fitting (lines) of the adsorption isotherms (points) of LIFM-66 measured at 273, 298 and 313 K.

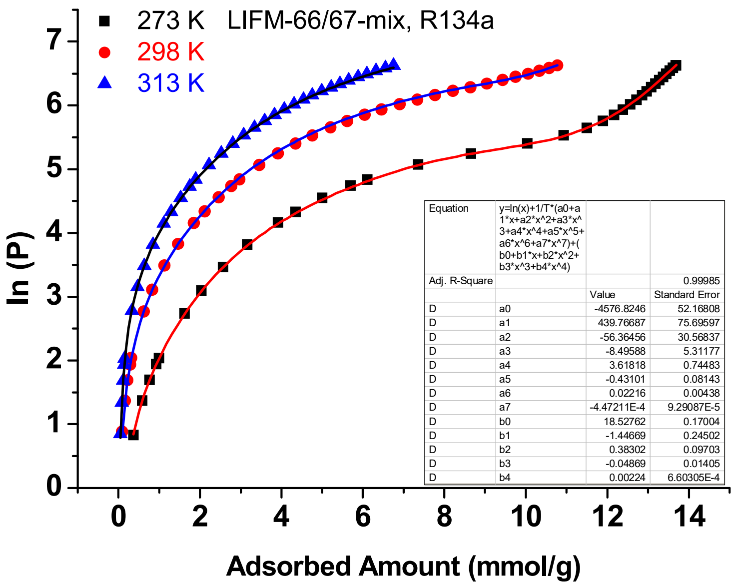

Figure S37. R134a fitting (lines) of the adsorption isotherms (points) of LIFM-66/67-mix measured at 273, 298 and 313 K.

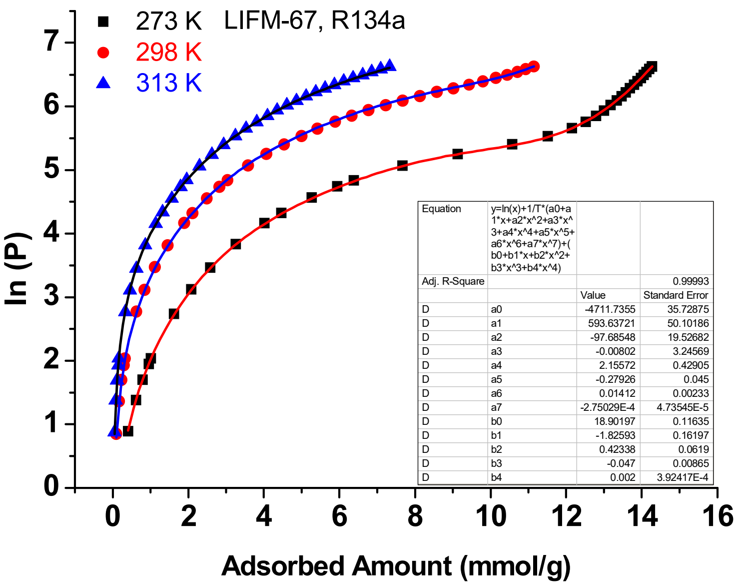

Figure S38. R134a fitting (lines) of the adsorption isotherms (points) of LIFM-67 measured at 273, 298 and 313 K.

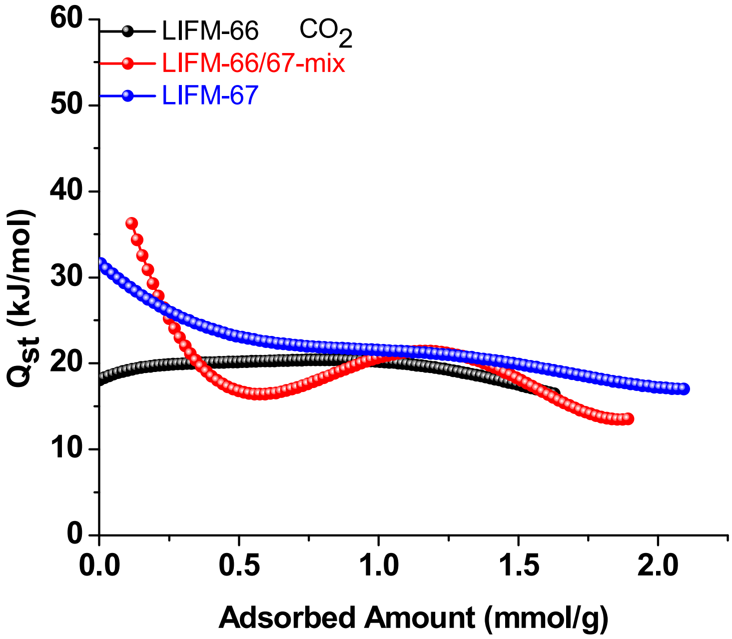

Figure S39. CO_2 isosteric heat of adsorption in LIFM-66, LIFM-66/67-mix and LIFM-67 as a function of surface coverage.

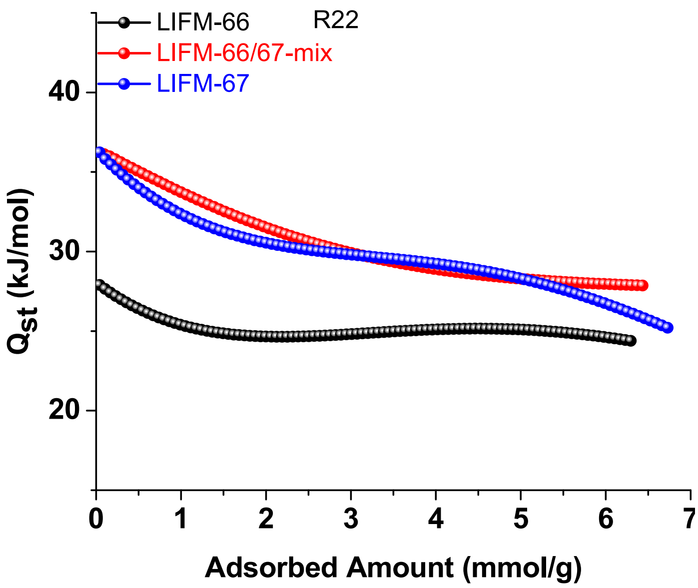

Figure S40. R22 isosteric heat of adsorption in LIFM-66, LIFM-66/67-mix and LIFM-67 as a function of surface coverage.

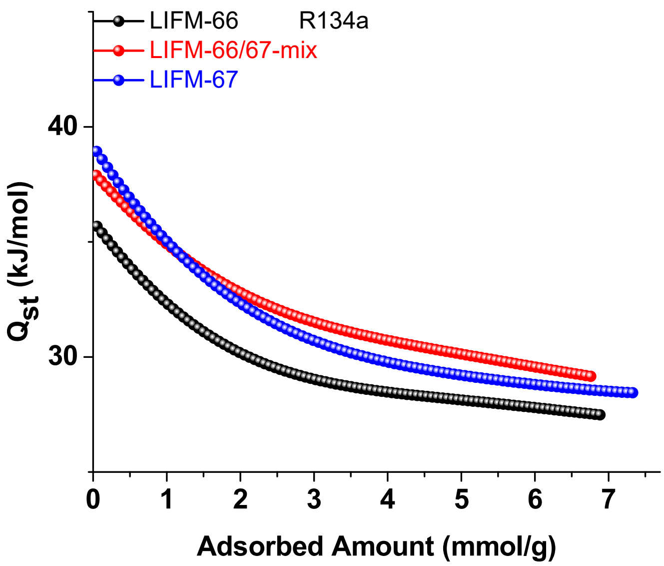

Figure S41. R134a isosteric heat of adsorption in LIFM-66, LIFM-66/67-mix and LIFM-67 as a function of surface coverage.

S12. CO_2/N_2, R22/N_2 and R134a/N_2 Selectivity Calculation via IAST

The experimental isotherm data for pure CO_2, R22, R134a, and N_2 (measured at 298 K) were fitted using a Langmuir Freundlich (LF) model:

$$q = \frac{a*b*p^{1/n}}{1+b*p^{1/n}} \quad \text{eq. 3}$$

Where q and p are adsorbed amounts and pressure of component i, respectively.

The adsorption selectivities for binary mixtures of C_2H_6/C_2H_4 defined by

$$S_{i/j} = \frac{x_i}{x_j} * \frac{y_j}{yi} \quad \text{eq. 4}$$

were calculated using the Ideal Adsorption Solution Theory (IAST) of Myers and Prausnitz.[19] Where x_i is the mole fraction of component i in the adsorbed phase and y_i is the mole fraction of component in the bulk.

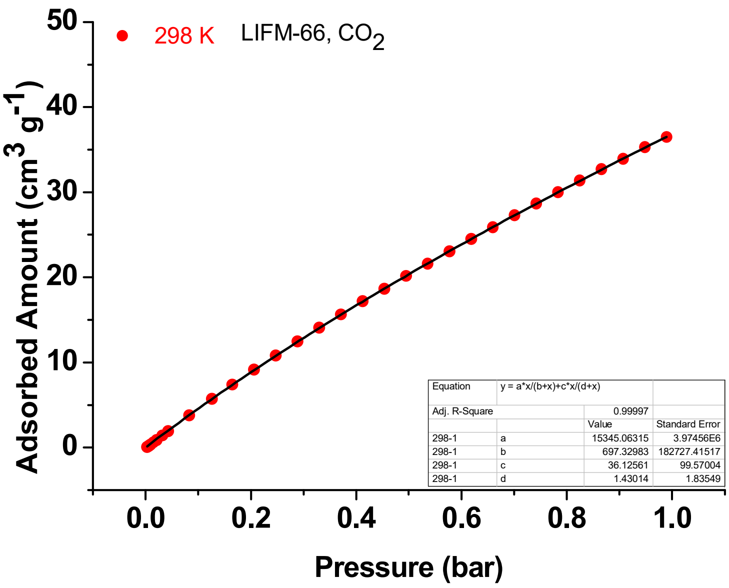

Figure S42. CO_2 adsorption isotherms of LIFM-66 with fitting by LF model.

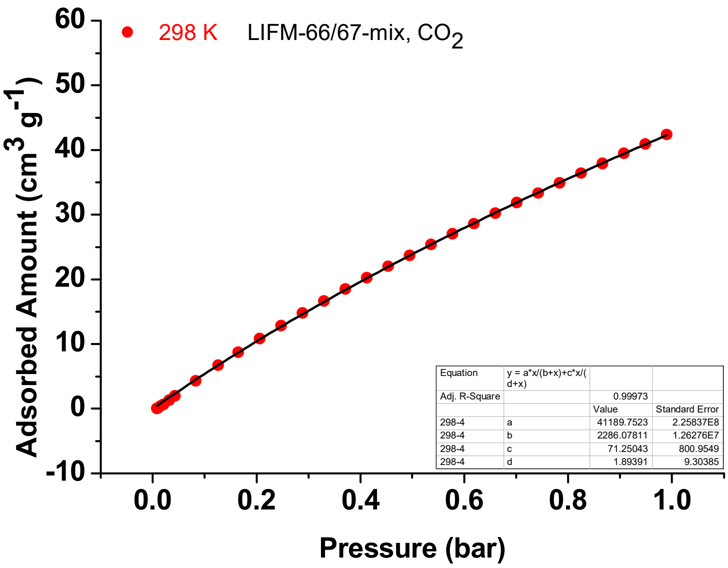

Figure S43. CO_2 adsorption isotherms of LIFM-66/67-mix with fitting by LF model.

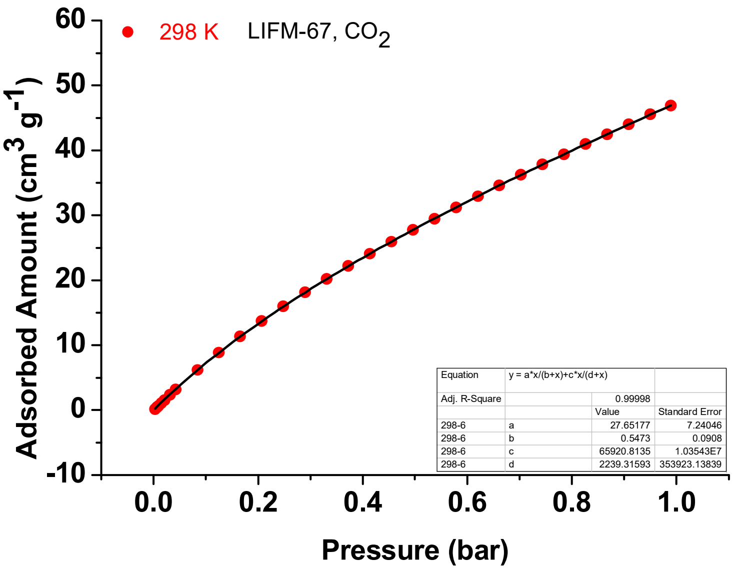

Figure S44. CO_2 adsorption isotherms of LIFM-67 with fitting by LF model.

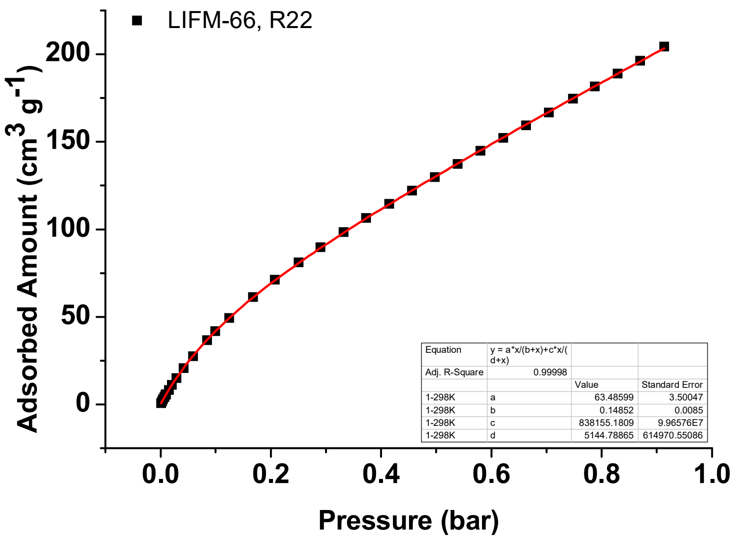

Figure S45. R22 adsorption isotherms of LIFM-66 with fitting by LF model.

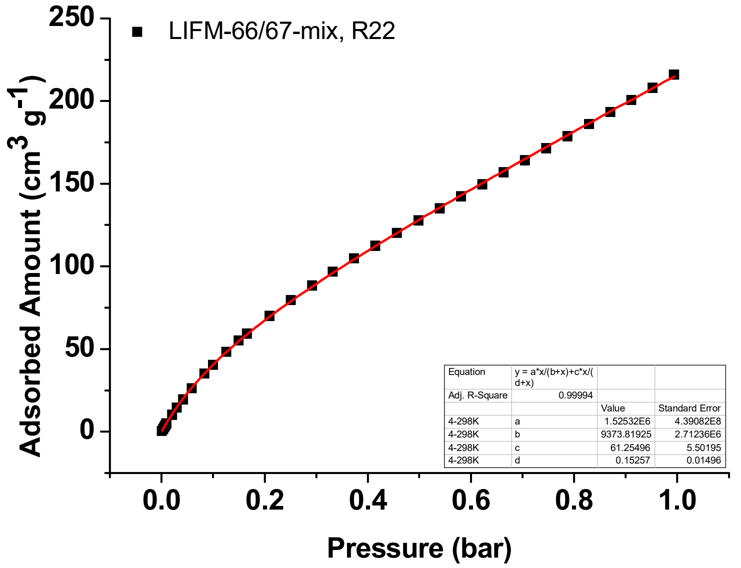

Figure S46. R22 adsorption isotherms of LIFM-66/67-mix with fitting by LF model.

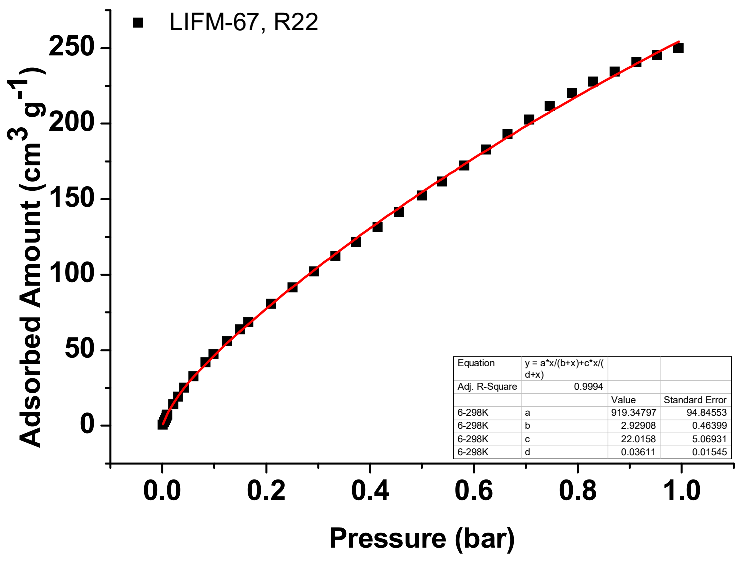

Figure S47. R22 adsorption isotherms of LIFM-67 with fitting by LF model.

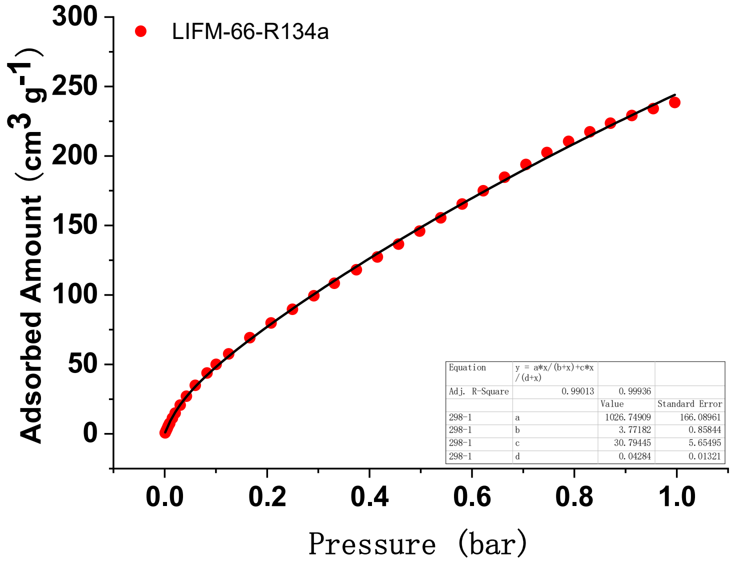

Figure S48. R134a adsorption isotherms of LIFM-66 with fitting by LF model.

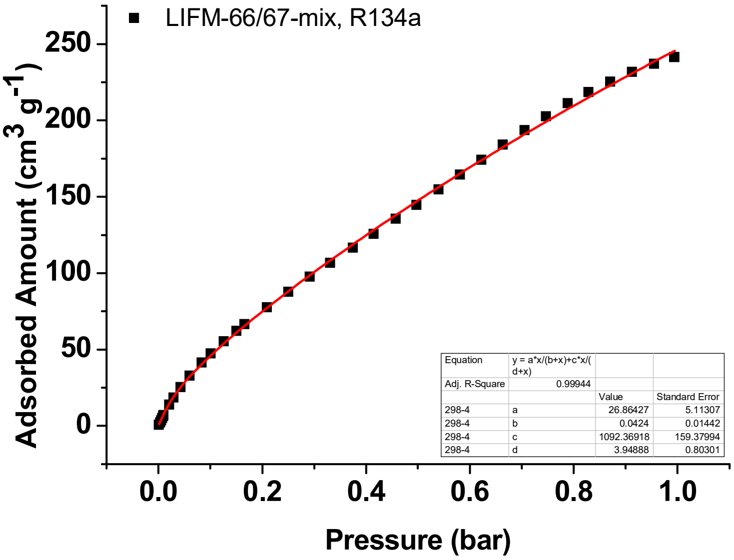

Figure S49. R134a adsorption isotherms of LIFM-66/67-mix with fitting by LF model.

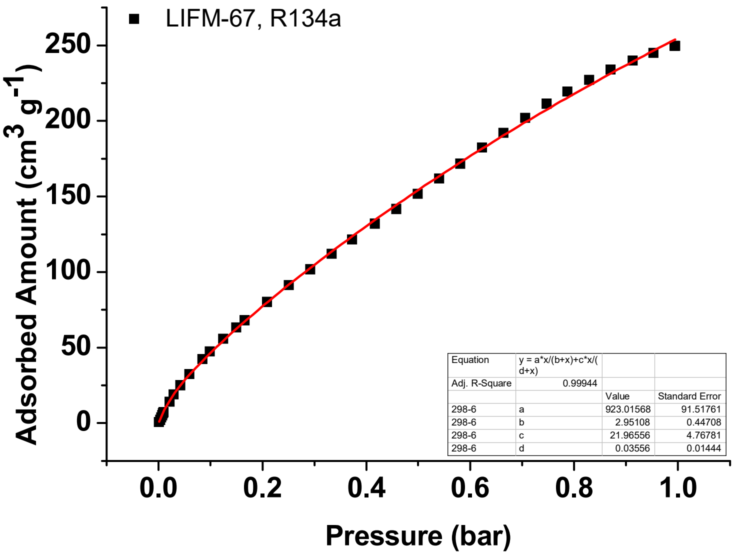

Figure S50. R134a adsorption isotherms of LIFM-67 with fitting by LF model.

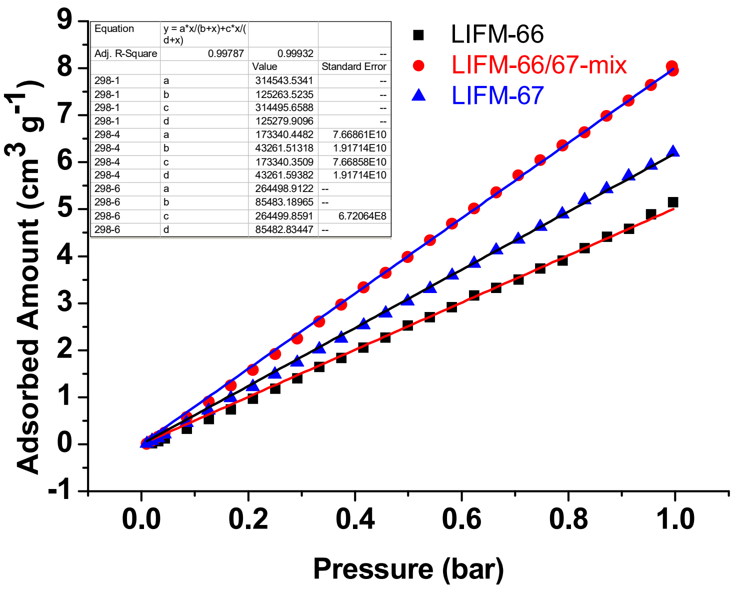

Figure S51. N_2 adsorption isotherms of LIFM-66, LIFM-66/67-mix and LIFM-67 with fitting by LF model.

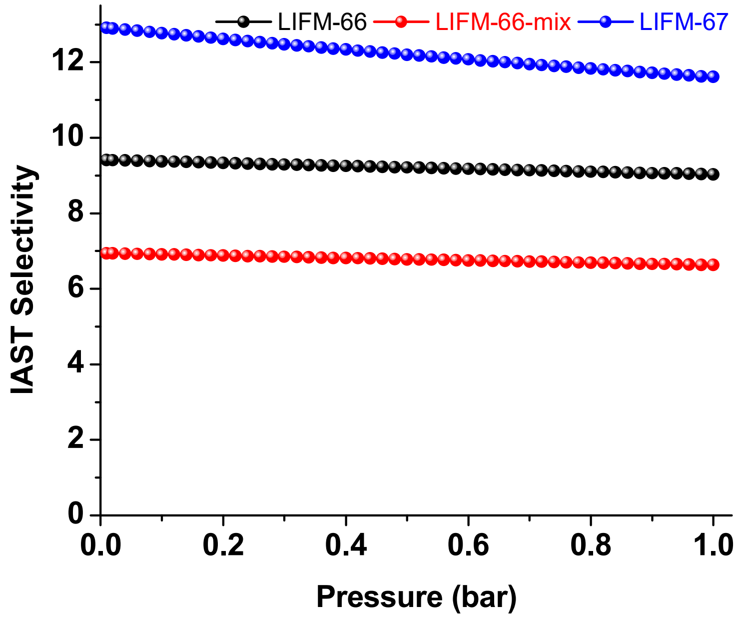

Figure S52. IAST calculative selectivity of CO_2/N_2 (15:85) on LIFM-66, LIFM-66/67-mix and LIFM-67 at 298 K.

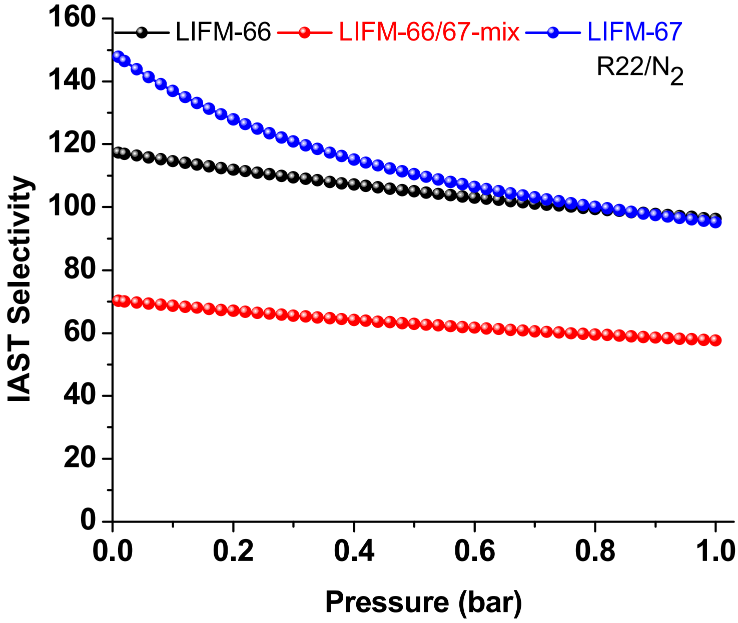

Figure S53. IAST calculative selectivity of R22/N_2 (10:90) on LIFM-66, LIFM-66/67-mix and LIFM-67 at 298 K.

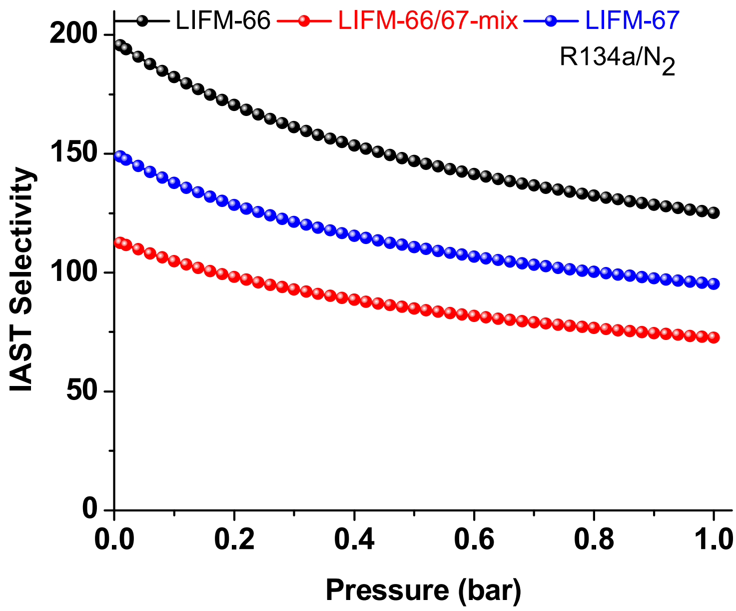

Figure S54. IAST calculative selectivity of R134a/N_2 (10:90) on LIFM-66, LIFM-66/67-mix and LIFM-67 at 298 K.

S13 Simulated transient breakthrough

13.1 Fitting of unary isotherm data

The unary isotherms at 298 K were fitted with good accuracy using the Langmuir-Freundlich model.

$$q = \frac{q_{sat} b p^{\nu}}{1 + b p^{\nu}}$$

Table S6. Langmuir-Freundlich parameter fits for LIFM-66.

Adsorbate	q_{sat} mol kg^{-1}	b Pa$^{-\nu}$	ν
R22	38	1.685E-05	0.86
R134a	48	2.054E-05	0.83
N_2	0.4	1.890E-08	1.56

Table S7. Langmuir-Freundlich parameter fits for LIFM-67.

Adsorbate	q_{sat} mol kg^{-1}	b Pa$^{-\nu}$	ν
R22	49	1.508E-05	0.86
R134a	50.5	1.620E-05	0.85
N_2	0.56	5.204E-08	1.45

13.2 Transient breakthrough simulations

Transient breakthrough simulations of the adsorption were carried out for binary 1/99 and 10/90 R22/N_2 and R134a/N_2 mixtures at a total pressure of 100 kPa and 298 K, using the methodology described in earlier publications.[20-24] In these simulations, intra-crystalline diffusion influences are ignored. Length of bed, L = 0.3 m; superficial gas velocity at the entrance to the bed, $u_0 = 0.04$ m s^{-1}; voidage of the packed bed, ε = 0.4. The interstitial gas velocity $v = \frac{u_0}{\varepsilon}$.

For presenting the breakthrough simulation results, we may use the dimensionless time, $\tau = \frac{tu}{L\varepsilon}$, obtained by dividing the actual time, t, by the characteristic time, $\frac{L}{v} = \frac{\varepsilon L}{u_0}$, where L is the length of adsorber, v is the interstitial gas velocity.

Notation

b: Langmuir-Freundlich constant, $\mathrm{Pa}^{-\nu}$; q: component molar loading of species i, mol kg^{-1}; q_{sat}: saturation loading, mol kg^{-1}; L: length of packed bed adsorber, m; t: time, s; T: absolute temperature, K; u: superficial gas velocity in packed bed, m s^{-1}; v: interstitial velocity in packed bed, m s^{-1}.

Greek letters

ε: voidage of packed bed, dimensionless; ν: Freundlich-exponent, dimensionless; τ: time, dimensionless.

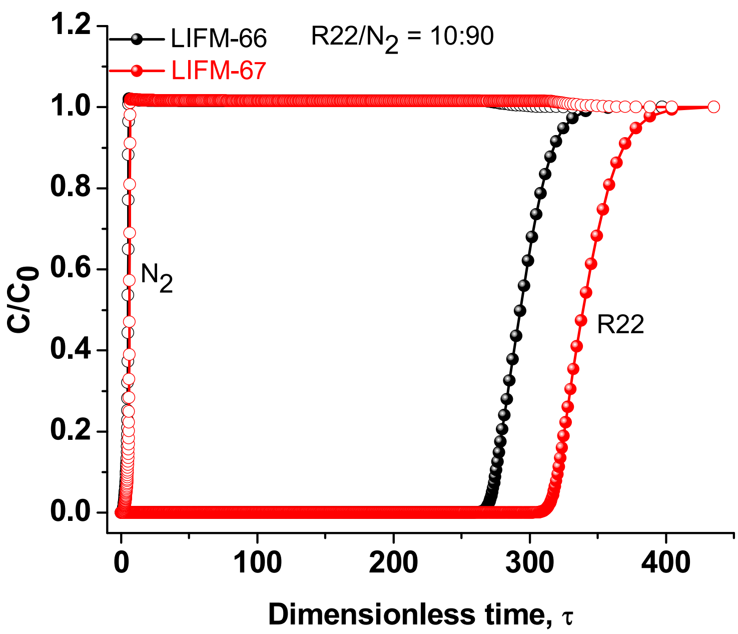

Figure S55. Transient breakthrough simulations for the separation of R22/N_2 (10:90) mixtures using LIFM-66/67 at 298 K, with a total pressure of 101 kPa.

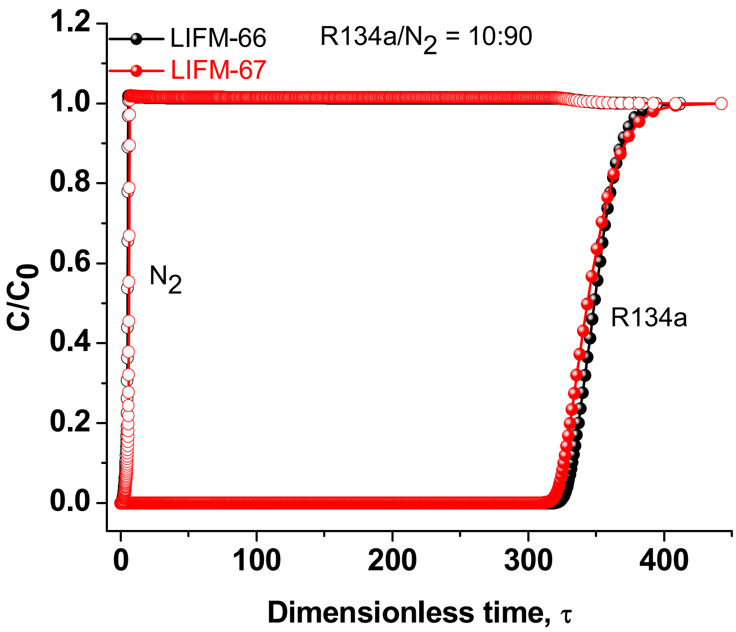

Figure S56. Transient breakthrough simulations for the separation of R134a/N_2 (10:90) mixtures using LIFM-66/67 at 298 K, with a total pressure of 101 kPa.

S14. Transient Breakthrough Experiments

The breakthrough experiments were carried out in a dynamic gas breakthrough set-up. All experiments were conducted using a stainless-steel column. According to the different particle size and density of the sample powder, the weight packed in the column was: 1.62 g for LIFM-66, 1.90 g for LIFM-67. Outlet gas from the column was monitored using a mass spectrometer (Pfeiffer GSD320). The mixed gas flow rate during breakthrough process is 20 mL min^{-1} for 1/99 (v/v) R134a/N_2 under 10 or 50 % humid conditions. After the breakthrough experiment, the sample was regenerated under N_2 flow.

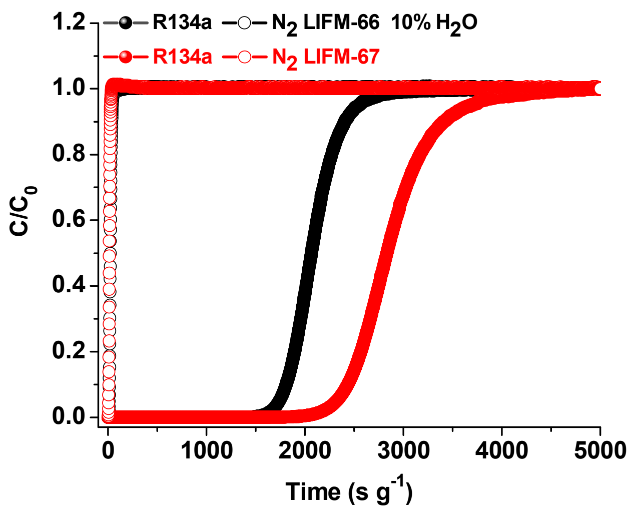

Figure S57. Transient breakthrough experiments for the separation of R134a/N_2 (1:99) mixtures using LIFM-66 and LIF-67 at 298 K under 10 % humid condition with a rate of 20 mL min^{-1}.

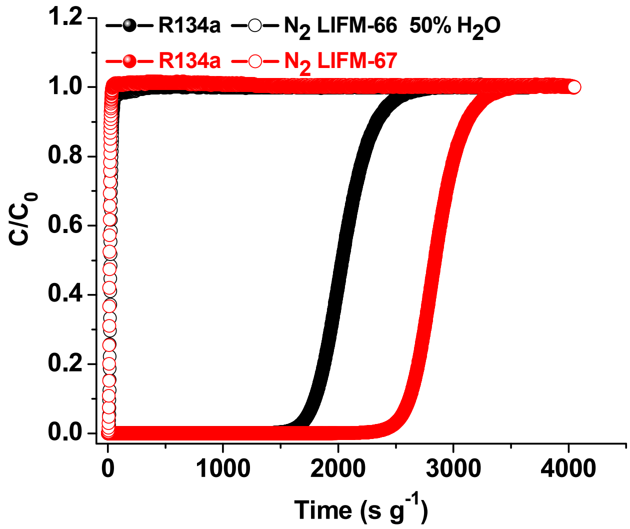

Figure S58. Transient breakthrough experiments for the separation of R134a/N_2 (1:99) mixtures using LIFM-66 and LIF-67 at 298 K under 50 % humid condition with a rate of 20 mL min^{-1}.

S15. Adsorption Kinetic

The adsorption kinetic experiments were carried out using a multi-station gravimetric gas/vapor adsorption instrument (BSD-VVS) through a gravimetric vacuum sorption method. In a typical adsorption kinetic experiment, the samples for LIFM-66, 66/67-mix, 67 were activated at 70 ºC for 12 h under high vacuum, then setted the pressure to 0.95 bar and saved the settings. Afterwards, the adsorptions were performed.

S16. Modeling Studies

The binding sites for $CHClF_2$ and CH_2FCF_3 in LIFM-66 and LIFM-67 were determined through classical molecular simulations. The single X-ray crystallographic structures that were published herein for the respective MOFs were used to perform the parametrizations and simulations.

All atoms of LIFM-66 and LIFM-67 were treated with Lennard-Jones (LJ) parameters (ε and σ),[25] point partial charges, and static point polarizabilities in order to model repulsion/dispersion, stationary electrostatic, and many-body polarization interactions, respectively. The LJ parameters for all aromatic C and H atoms were taken from the Optimized Potentials For Liquid Simulations – All Atom (OPLS-AA) force field,[26] while those for all other atoms were taken from the Universal Force Field (UFF).[27] The partial charges for the unique atoms in LIFM-66 and LIFM-67 were determined through the extended charge equilibration (EQ_{eq}) method.[28] The exponential damping-type polarizability values for all C, H, and O atoms were taken from a carefully parametrized set provided by the work of van Duijnen and Swart.[29] For Zr^{4+}, the polarizability value that was reported in the work of Shannon and Fischer[30] was utilized.

In order to develop a model for $CHClF_2$ and CH_2FCF_3, the atomic positions of both adsorbates were first optimized at the Hartree–Fock level of theory with the aug-cc-pVQZ basis set[31] assigned to all atoms using the NWChem *ab initio* software.[32] Afterward, the electrostatic potential surface of the molecules were calculated using the same level of theory and basis set that were employed for the optimizations, and partial charges were subsequently fitted onto the atomic positions of the respective adsorbates using the CHELPG method.[33] These partial charges were utilized for the atoms in both adsorbates for the classical simulations. All C, H, F, and Cl atoms in these optimized molecules were assigned LJ parameters from the UFF[27] and the exponential damping-type polarizability values from the work of van Duijnen and Swart.[29]

Simulated annealing (SA) calculations[34] were performed for a single molecule of each adsorbate through a canonical Monte Carlo (CMC) process in a unit cell of LIFM-66 and LIFM-

67. All MOF atoms were kept fixed at their crystallographic positions throughout the simulations. A spherical cut-off distance corresponding to half the shortest unit cell dimension length was used for the simulations in both MOFs. The total potential energy of the MOF-adsorbate system was calculated through the sum of the repulsion/dispersion, stationary electrostatic, and many-body polarization energies. These were calculated using the LJ potential,[25] the Ewald summation technique,[35] and a Thole-Applequist type model,[36] respectively. SA calculations for each adsorbate utilized an initial temperature of 500 K, and this temperature was scaled by a factor of 0.99999 after every 10^3 Monte Carlo (MC) steps. The simulations continued until 10^6 MC steps were reached; at this point, the temperature of the system is below 25 K and the adsorbate is already localized in its energy minimum position in the MOF. All simulations were carried out using the Massively Parallel Monte Carlo (MPMC) code.[37]

Next, CMC simulations[38] were performed for a single molecule of $CHClF_2$ and CH_2FCF_3, individually, positioned at their global minimum in LIFM-66 and LIFM-67. This was done in order to evaluate the averaged classical potential energy for both adsorbates about their energy minimum position in the material. The CMC simulations were performed at a temperature of 20 K and a pressure of 1.0 atm. These simulations ran for a total of 10^6 MC steps to ensure reasonable ensemble averages for the total potential energy of the system. The averaged classical potential energies for $CHClF_2$ and CH_2FCF_3 localized about their energy minimum position in LIFM-66 and LIFM-67 are presented in Table S8.

Table S8. Calculated averaged total potential energies (in kJ mol^{-1}) for a single $CHClF_2$ and CH_2FCF_3 molecule, individually, positioned at their global minimum in LIFM-66 and LIFM-67 as determined from CMC simulations at 20 K/1.0 atm.

MOF	Adsorbate	MOF-Adsorbate Energy (kJ mol^{-1})
LIFM-66	$CHClF_2$	–35.5
	CH_2FCF_3	–45.1
LIFM-67	$CHClF_2$	–42.8
	CH_2FCF_3	–46.7

S17. Reference

1 Z. W. Wei, Z. Y. Gu, R. K. Arvapally, Y. P. Chen, R. N. McDougald, J. F. Ivy, A. A. Yakovenko, D. W. Feng, M. A. Omary and H. C. Zhou, *J. Am. Chem. Soc.*, 2014, **136**, 8269-8276.

2 B. Wang, X.-L. Lv, D. Feng, L.-H. Xie, J. Zhang, M. Li, Y. Xie, J.-R. Li and H.-C. Zhou, *J. Am. Chem. Soc.*, 2016, **138**, 6204-6216.

3 C. X. Chen, Z. W. Wei, Y. N. Fan, P. Y. Su, Y. Y. Ai, Q. F. Qiu, K. Wu, S. Y. Yin, M. Pan and C. Y. Su, *Chem*, 2018, **4**, 2658-2669.

4 G. M. Sheldrick, *Acta Crystallogr A* **2008**, *64*, 112-122.

5 (a) A. L. Spek., *J. Appl. Cryst.* **2003**, *36*, 7-13; (b) A. L. Spek, *Acta Crystallogr. D* **2009**, *65*, 148-155; (c) A. L. Spek, *Acta Crystallogr. C* **2015**, *71*, 9-18.

6 R. K. Motkuri, H. V. R. Annapureddy, M. Vijaykumar, H. T. Schaef, P. F. Martin, B. P. McGrail, L. X. Dang, R. Krishna and P. K. Thallapally, *Nat. Commun.*, **2014**, *5*.

7 R. B. Lin, T. Y. Li, H. L. Zhou, C. T. He, J. P. Zhang and X. M. Chen, *Chem. Sci.*, **2015**, *6*, 2516-2521.

8 C. X. Chen, S. P. Zheng, Z. W. Wei, C. C. Cao, H. P. Wang, D. W. Wang, J. J. Jiang, D. Fenske and C. Y. Su, *Chem. Eur. J.*, **2017**, *23*, 4060-4064.

9 C. X. Chen, Z. Wei, J. J. Jiang, Y. Z. Fan, S. P. Zheng, C. C. Cao, Y. H. Li, D. Fenske and C. Y. Su, *Angew. Chem. Int. Ed.*, **2016**, *55*, 9932-9936.

10 C. X. Chen, Z. W. Wei, J. J. Jiang, S. P. Zheng, H. P. Wang, Q. F. Qu, C. C. Cao, D. Fenske and C. Y. Su, *J. Am. Chem. Soc.*, **2017**, *139*, 6034-6037.

11 C. X. Chen, Q. F. Qiu, C. C. Cao, M. Pan, H. P. Wang, J. J. Jiang, Z. W. Wei, K. Zhu, G. Q. Li and C. Y. Su, *Chem. Commun.*, **2017**, *53*, 11403-11406.

12 J. Zheng, R. S. Vemuri, L. Estevez, P. K. Koech, T. Varga, D. M. Camaioni, T. A. Blake, B. P. McGrail and R. K. Motkuri, *J. Am. Chem. Soc.*, **2017**, *139*, 10601-10604.

13 J. Zheng, D. Barpaga, B. A. Trump, M. Shetty, Y. Fan, P. Bhattacharya, J. J. Jenks, C. Y. Su, C. M. Brown, G. Maurin, B. P. McGrail and R. K. Motkuri, *J. Am. Chem. Soc.*, **2020**, *142*, 3002-3012.

14 Z. W. Mo, H. L. Zhou, D. D. Zhou, R. B. Lin, P. Q. Liao, C. T. He, W. X. Zhang, X. M. Chen and J. P. Zhang, *Adv. Mater.*, **2018**, *30*.

15 T. H. Chen, I. Popov, W. Kaveevivitchai, Y. C. Chuang, Y. S. Chen, A. J. Jacobson and O. S. Miljanic, *Angew. Chem. Int. Ed.*, **2015**, *54*, 13902-13906.

16 J. Zheng, D. Barpaga, O. Y. Gutiérrez, N. D. Browning, B. L. Mehdi, O. K. Farha, J. A. Lercher, B. P. McGrail, R. K. Motkuri, *ACS Appl. Energy Mater.* **2018**, *1*, 5853-5858.

17 J. Zheng, M. Wahiduzzaman, D. Barpaga, B. A. Trump, O. Y. Gutiérrez, P. Thallapally, S. Ma, B. P. McGrail, G. Maurin, R. K. Motkuri, *Angew. Chem. Int. Ed.* **2021**, *60*, 18037-18043

18 J. J. L. Czepirski, *Chem. Eng. Sci.*, 1989, **44**, 797-801.

19 A. L. Myers and M. Prausnitz, *J. AIChE.*, **1965**, *11*, 121-127.

20 R. Krishna, *Microporous Mesoporous Mater.* **2014**, *185*, 30-50.

21 R. Krishna, *RSC Adv.* **2015**, *5*, 52269-52295.

22 R. Krishna, *RSC Adv.* **2017**, *7*, 35724-35737.

23 R. Krishna, *Sep. Purif. Technol.* **2018**, *194*, 281-300.

24 R. Krishna, *ACS Omega* **2020**, *5*, 16987−17004.

25 J. E. Jones, *Proc. R. Soc. A* **1924**, *106*, 463–477.

26 W. L. Jorgensen, D. S. Maxwell, J. Tirado-Rives, *J. Am. Chem. Soc*. **1996**, *118*, 11225–11236.

27 A. K. Rappé, C. J. Casewit, K. S. Colwell, W. A. Goddard, W. M. Skiff, *J. Am. Chem. Soc*. **1992**, *114*, 10024–10035.

28 C. E. Wilmer, K. C. Kim, R. Q. Snurr, *J. Phys. Chem. Lett*. **2012**, *3*, 2506–2511.

29 P. T. Van Duijnen, M. *J.* Swart, *Phys. Chem. A* **1998**, *102*, 2399–2407.

30 R. D. Shannon, R. X. Fischer, *Am. Mineral*. **2016**, *101*, 2288–2300.

31 (a) T. H. Dunning, *J. Chem. Phys*. **1989**, *90*, 1007–1023. (b) R. A. Kendall, T. H. Dunning, R. J. Harrison, *J. Chem. Phys*. **1992**, *96*, 6796–6806. (c), D. E. Woon, T. H. Dunning, *J. Chem. Phys*. **1993**, *98*, 1358–1371.

32 M. Valiev, E. Bylaska, N. Govind, K. Kowalski, T. Straatsma, H. V. Dam, D. Wang, J.; Apra, E. Nieplocha, T. Windus, W. De Jong, *Comput. Phys. Commun*. **2010**, *181*, 1477–1489.

33 (a) L. E. Chirlian, M. M. Francl, *J. Comput. Chem*. **1987**, *8*, 894–905. (b) C. M. Breneman, K. B. Wiberg, *J. Comput. Chem*. **1990**, *11*, 361–373.

34 S. Kirkpatrick, C. D. Gelatt, M. P. Vecchi, *Science* **1983**, *220*, 671−680.

35 (a), P. P. Ewald, *Ann. Phys*. **1921**, *369*, 253–287. (b) B. A. Wells, A. L. Chaffee, *J. Chem. Theory Comput*. **2015**, *11*, 3684–3695.

36 (a) J. Applequist, J. R. Carl, K. K. Fung, *J. Am. Chem. Soc*. **1972**, *94*, 2952−2960. (b) B. Thole, *Chem. Phys*. **1981**, *59*, 341−350. (c) K. A. Bode, J. Applequist, *J. Phys. Chem*. **1996**, *100*, 17820−17824. (d) K. McLaughlin, C. R. Cioce, T. Pham, J. L. Belof, B. Space, *J. Chem. Phys*. **2013**, *139*, 184112.

37 (a) J. L. Belof, B. Space, *Massively Parallel Monte Carlo (MPMC)*. 2012, Available on GitHub. https://github.com/mpmccode/mpmc. (b) D. M. Franz, J. L. Belof, K. McLaughlin, C. R. Cioce, B. Tudor, A. Hogan, L. Laratelli, M. Mulcair, M. Mostrom, A. Navas, A. C. Stern, K. A. Forrest, T. Pham, B. Space, *Adv. Theory Simul*. **2019**, *2*, 1900113.

38 D. Frenkel, B. Smit, *Understanding Molecular Simulation: From Algorithms to Applications*; Academic Press: New York, 2002; Chapter 5, Section 5.2, pp 112–114.